12-1-2010

Novel Approaches to Image Segmentation Based on Neutrosophic Logic

Ming Zhang
Utah State University

NOVEL APPROACHES TO IMAGE SEGMENTATION

BASED ON NEUTROSOPHIC LOGIC

by

Ming Zhang

A dissertation submitted in partial fulfillment
of the requirements for the degree

of

DOCTOR OF PHILOSOPHY

in

Computer Science

Approved:

_____   _____
Dr. Heng-Da Cheng   Dr. Xiaojun Qi
Major Professor   Committee Member

_____   _____
Dr. Daniel W. Watson   Dr. Stephen J. Allan
Committee Member   Committee Member

_____   _____
Dr. YangQuan Chen   Dr. Byron R. Burnham
Committee Member   Dean of Graduate Studies

UTAH STATE UNVIERSITY
Logan, Utah

2010

ABSTRACT

Novel Approaches to Image Segmentation

Based on Neutrosophic Logic

by

Ming Zhang, Doctor of Philosophy

Utah State University, 2010

Major Professor: Dr. Heng-Da Cheng
Department: Computer Science

Neutrosophy studies the origin, nature, scope of neutralities, and their interactions with different ideational spectra. It is a new philosophy that extends fuzzy logic and is the basis of neutrosophic logic, neutrosophic probability, neutrosophic set theory, and neutrosophic statistics.

Because the world is full of indeterminacy, the imperfection of knowledge that a human receives/observes from the external world also causes imprecision. Neutrosophy introduces a new concept <Neut-A>, which is the representation of indeterminacy. However, this theory is mostly discussed in physiology and mathematics. Thus, applications to prove this theory can solve real problems are needed.

Image segmentation is the first and key step in image processing. It is a critical and essential component of image analysis and pattern recognition. In this dissertation, I apply neutrosophy to three types of image segmentation: gray level images, breast ultrasound images, and color images. In gray level image segmentation, neutrosophy

helps reduce noise and extend the watershed method to normal images. In breast ultrasound image segmentation, neutrosophy integrates two controversial opinions about speckle: speckle is noise versus speckle includes pattern information. In color image segmentation, neutrosophy integrates color and spatial information, global and local information in two different color spaces: RGB and CIE ($L^*u^*v^*$), respectively. The experiments show the advantage of using neutrosophy.

(106 pages)

This work is dedicated to my family,
my wife, Yuan Zhang.

ACKNOWLEDGMENTS

First, I would like to thank Dr. Heng-Da Cheng, my advisor, for his direction and encouragement of my research. I appreciate his great help in completing this dissertation. I would like to thank my committee members, Dr. Xiaojun Qi, Dr. Dan Watson, Dr. Steve Allan, and Dr. YangQuan Chen, for their inspiration, comments, and advice throughout my entire research.

I also express my thanks to the members of the CVPRIP group, Juan Shan, Yuxuan Wang, Yanhui Guo, and Chenguang Liu.

Particularly, I wish to thank my wife, Yuan Zhang. Although geographical distance has separated us during much of my research, she continually encourages, supports, and loves me.

Ming Zhang

CONTENTS

LIST OF TABLES

LIST OF FIGURES

CHAPTER 1

INTRODUCTION

Neutrosophy is a branch of philosophy that combines the knowledge of philosophy, logics, set theory, and probability/statistics [1]. Neutrosophy introduces a new concept called <Neut-A> which represents indeterminacy. It can solve certain problems that cannot be solved by fuzzy logic [2]. For example, a paper is sent to two reviewers, both of whom claim the paper as 90% acceptable. But the two reviewers may have different backgrounds. One is an expert, and another is a new comer in this field. The impacts on the final decision of the paper by the two reviewers should be different, even though they give the same grade level of the acceptance. There are many similar problems, such as weather forecasting, stock price prediction, and political elections, containing indeterminate conditions that fuzzy logic does not handle well [3].

1.1 Neutrosophy

The word neutrosophy, taken from the Latin 'neuter'—neutral, Greek 'sophia'—skill/wisdom was introduced by Smarandache in 1980 [4]. It is a generalization of fuzzy logic based on the proposition that t true, i indeterminate, and f false. t, i and f are real values from the ranges T, I, F, with no restrictions on them. The following are the examples of different types of logic [4]:

1. Intuitionistic logic, which supports incomplete theories (for $0 < n < 100,\ 0 \le t,\ i,\ f \le 100$).

2. Fuzzy logic (for $n = 100$, $i = 0$, and $0 \le t, f \le 100$).

3. Boolean logic (for $n = 100$, $i = 0$, with t, f either 0 or 100).

4. Paraconsistent logic (for $n > 100$, with both $t, f < 100$)

5. Dialetheism (for $t = f = 100$ and $i = 0$)

The following two examples help illustrate how neutrosophy, a generalization of fuzzy logic, is closer to human reasoning than other forms of logic.

1. When we say "tomorrow it will be raining," we do not mean a fixed-valued. In neutrosophic terms, we may say the statement is 60% true, 50% indeterminate and 30% false.

2. The truth value also depends/changes with respect to the observer. The statement "Tom is smart," can be (0.35, 0.67, 0.6) according to his boss, (0.8, 0.25, 0.1) according to himself, or (0.5, 0.2, 0.3) according to his wife.

Neutrosophy is closer to human reasoning because, like the human mind, it characterizes/catches the imprecision of knowledge or linguistic inexactitude received by various observers. The uncertainty may derive from incomplete knowledge, acquisition errors, or stochasticity [5].

Neutrosophy is the basis of neutrosophic logic, a multiple value logic that generalizes fuzzy logic, classical logic, and imprecise probability.

1.2 Neutrosophic Sets

A neutrosophic set is a generalization of an intuitionistic set, fuzzy set, paraconsistent set, dialetheist set, paradoxist set, and a tautological set [1, 3, 6-8].

Define <A> as an event or entity, <Non-A> is not <A>, and <Anti-A> is the opposite of <A>. Also, <Neut-A> is defined as neither <A> nor <Anti-A>. For example, if <A> = white, then <Anti-A> = black. <Non-A> = blue, yellow, red, black, etc. (any color except white). <Neut-A> = blue, yellow, red, etc. (any color except white and black).

Define T, I, and F as neutrosophic components to represent <A>, <Neut-A>, and <Anti-A>. Let T, I, and F be standard or non-standard real subsets of $]^-0, 1^+[$ with $\sup T = t\_sup$, $\inf T = t\_inf$, $\sup I = i\_sup$, $\inf I = i\_inf$, $\sup F = f\_sup$, $\inf F = f\_inf$ and $n\_sup = t\_sup + i\_sup + f\_sup$, $n\_inf = t\_inf + i\_inf + f\_inf$ [9]. x_sup specifies the superior limits of the subsets, and x_inf specifies the inferior limits of the subsets. T, I, and F are not necessarily intervals, but may be any real sub-unitary subsets. T, I, and F are set-valued vector functions or operations depending on known or unknown parameters, and they may be continuous or discrete. Additionally, they may overlap or be converted from one to the other [1]. An element $A(T, I, F)$ belongs to the set in the following way: it is t true ($t \in T$), i indeterminate ($i \in I$), and f false ($f \in F$), where t, i, and f are real numbers in the sets T, I and F. Figure 1.1 is the relationship among a neutrosophic set and other sets. In a classical set, $I = \phi, \inf T = \sup T = 0 \, or \, 1, \, \inf F = \sup F = 0 \, or \, 1 \, and \, \sup T + \sup F = 1$. In a fuzzy set, $I = \phi, \inf T = \sup T \in [0,1]$, $\inf F = \sup F \in [0,1] \, and \, \sup T + \sup F = 1$. In a neutrosophic set, $I, T, F \in]0^-, 1^+[$.
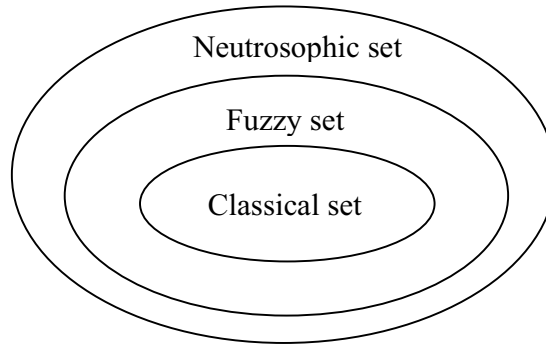
Figure 1.1. Relationships among neutrosophic set and other sets.

In order to apply neutrosophy, an image needs to be transferred to a neutrosophic domain. A pixel in the neutrosophic domain can be represented as $P\{T, I, F\}$, meaning the pixel is $t\%$ true, $i\%$ indeterminate, and $f\%$ false, where t varies in T, i varies in I, and f varies in F, respectively. In a classical set, $i = 0$, t and f are either 0 or 100. In a fuzzy set, $i = 0$, $0 \le t, f \le 100$. In a neutrosophic set, $0 \le t, i, f \le 100$.

1.3 Operations with Neutrosophic Sets

Let S_1, S_2 be two neutrosophic sets. Then we define:

- Addition

$$S_1 \oplus S_2 = \{x \mid x = s_1 + s_2, where\ s_1 \in S_1\ and\ s_2 \in S_2\}$$
$$with\ inf\ S_1 \oplus S_2 = inf\ S_1 + inf\ S_2, sup\ S_1 \oplus S_2 = sup\ S_1 + sup\ S_2$$

- Subtraction

$$S_1 \Theta S_2 = \{x \mid x = s_1 - s_2, where\ s_1 \in S_1\ and\ s_2 \in S_2\}$$
$$with\ inf\ S_1 \Theta S_2 = inf\ S_1 - inf\ S_2, sup\ S_1 \Theta S_2 = sup\ S_1 - sup\ S_2$$

- Multiplication

$$S_1 \odot S_2 = \{x \mid x = s_1 \bullet s_2, \text{ where } s_1 \in S_1 \text{ and } s_2 \in S_2\}$$
$$\text{with inf } S_1 \odot S_2 = \text{inf } S_1 \bullet \text{inf } S_2, \text{sup } S_1 \odot S_2 = \text{sup } S_1 \bullet \text{sup } S_2$$

- Division of a set by a number

$$\text{Let } k \in R, \quad S_1 \oslash k = \{x \mid x = s_1 / k, \text{ where } s_1 \in S_1\}$$

1.4 Image Segmentation

Image segmentation is a process to identify homogeneous regions in a given image [10]. It is typically used to locate objects and boundaries (lines, curves, and regions). In order to understand an image, we need isolate the objects in it and find relationships among them [11]. The goal of segmentation is to make the representation of an image more meaningful and easier to analyze [12]. Image segmentation can be defined as a process that divides an image into different regions. Each region is homogeneous, but the union of any two adjacent regions is not homogeneous.

Image segmentation is one of the most critical tasks of image analysis, and the quality of segmentation affects the subsequent process of image analysis and understanding, such as object representation and description, feature measurement, object classification, scene interpretation, etc. [13-18]. Moreover, it plays an important role in a variety of applications such as robot vision, object recognition, and medical imaging. It is defined as a bridge between a low level vision subsystem and a high level vision subsystem [19]. Figure 1.2 illustrates the flowchart of image processing.

Image segmentation is one of the most difficult tasks in the image processing field, because many features, such as intensity, blurring, contrast, and the number of segments,

Input Image

↓

| Image Preprocessing |

↓

| Image Segmentation |

↓

| Feature Extraction & Selection |

↓

| Classification |

↓

Evaluation
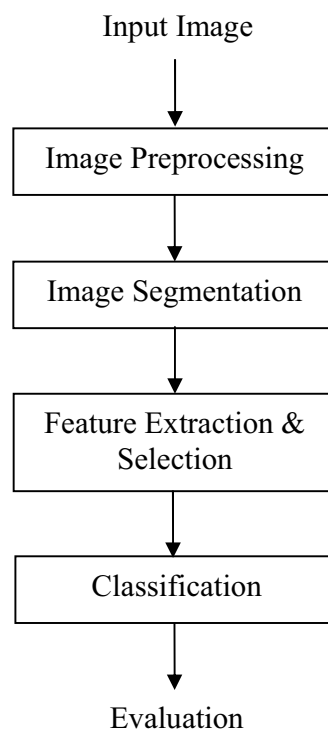
Figure 1.2. Flowchart of image processing.

affect the quality of segmentation. It is hard to extract all meaningful objects correctly and precisely from an image without any human interaction or supervision [20].

Image segmentation is divided into gray image segmentation and color image segmentation. Many algorithms and models of gray image segmentation can be modified and applied to color image segmentation. The more popular segmentation approaches are: histogram-based methods, edge-based methods, region-based methods, model-based methods, watershed methods, and fuzzy logic methods [16, 18, 21-23].

In this dissertation, neutrosophy is applied to gray images, breast ultrasound images, and color images. In gray image segmentation, I present a definition of T, I, F and use

neutrosophic logic to do the segmentation. In breast ultrasound image segmentation, I used a statistical evaluation to show the advantage of using neutrosophy. Because neutrosophy is an extension of fuzzy logic, I used neutrosophy in color image segmentation and compare it with different fuzzy logic methods to show the advantage of neutrosophy.

CHAPTER 2

GRAY LEVEL IMAGE SEGMENTATION

BASED ON NEUTROSOPHY

2.1 Introduction

Image segmentation is one of the most important parts in image processing. Most of applications that use images, such as object recognition, scene understanding and analysis, pattern recognition, remote sensing, medical image system, include this step.

2.1.1 Comparison of Different Segmentation Methods

A gray image is a simple kind of image that only contains one domain, and each pixel in the image can be represented by an integer $[0, 255]$. The most often used gray image segmentation algorithms are: the histogram-based algorithm [24-25], edge-based algorithm [26-27], region-based algorithm [28-29], model-based algorithm [30-31], and the watershed algorithm [32-33]. Table 2.1 gives a comparison of these algorithms.

Histogram-based techniques are relatively easy to compare with other segmentation methods. Such a technique first calculates a histogram of all pixels in an image and finds the peaks and valleys. Next, refinement algorithms are applied for further processing [12].

The edge-based method is one of the most common approaches for detecting discontinuities. First and second order derivatives like gradient and Laplacian are used to detect edges. Edges in an image can generally be divided into two categories: intensity

Table 2.1. Comparison of Segmentation Methods.

Method	Description	Advantage	Disadvantage
Histogram-based	Finds peaks and valleys in the histogram of the image and locates the clusters in the image.	Fast and simple.	Difficult to identify significant peaks and valleys.
Edge-based	Finds region boundaries.	Fast and well-developed.	Edges are often disconnected.
Region-based	Uses seeded region growing method.	Resulting regions are connected.	The choice of seeds is important and critical.
Model-based	Finds the interesting regions by using geometry.	Finds certain- shaped regions.	The regions need to fit a certain model.
Watershed	Considers image as topographic surface.	No seed is needed. Resulting regions are connected. Can find optimal boundaries.	Sensitive to noise and non-homogeneity.

edges and texture edges [34]. Intensity edges are from abrupt changes in the intensity profile of the image. Texture edges are boundaries of texture regions that are invariant to lighting conditions. Because non-uniform illumination or noise may affect intensity discontinuities, edge-based methods often have edge discontinuity problems.

Region-based methods include region growing and region splitting-merging procedures. Region growing groups pixels, or subregions, into larger regions. Initially, it requires a set of "seed" points. Regions grow up from these seeds if neighboring pixels have properties similar to those of the seed points. Selection of seeds is a critical procedure. In region splitting-merging, an image is subdivided into arbitrary, disjointed regions. These regions are merged and/or split to satisfy prerequisite constraints [10].

Model-based techniques locate object boundaries by employing physical models. Physical models are highly dependent on the nature of the materials present in the image. Existing model-based techniques are efficient in image processing only for materials whose reflection properties are known and easy to model. There are too many rigid assumptions of physical models regarding material type, light source, and illumination. These conditions might not be satisfied in the real world. Therefore, these techniques are only used in a very limited scope of applications.

Watershed techniques consider the gradient magnitude of an image as a topographic surface. Pixels having the highest gradient magnitude intensities correspond to watershed lines, which represent region boundaries. Water placed on a watershed line flows downhill to a common local intensity minima. Pixels draining to a common minimum form a catchments basin, which represents the regions. Direct application of this segmentation algorithm generally leads to over-segmentation due to noise and other local irregularities of the gradient.

In this chapter, I compare my proposed approach with the pixel-based method (embedded confidence), edge-based method (Sobel), region-based method (mean-shift), and two watershed methods (watershed in Matlab and toboggan-based).

2.1.2 Watershed Method

The original idea of the watershed method came from geography [21]. It is a powerful and popular image segmentation method [35-38] that can potentially provide more accurate segmentation with low computation cost [39]. A watershed algorithm splits an image into areas based on the topology of the image. The value of the gradients

is interpreted as the elevation information. After successively flooding the gray value, the watersheds with adjacent catchment basins are constructed. Figure 2.1(a) is an image with two dark blobs synthetically generated by Matlab, and (b) is the 3D watershed image obtained by applying the watershed method on (a). Because watershed methods work better on uniform images, my approach mainly deals with uniform images with blurry edges. However, my watershed method can also work better on non-uniform images than other watershed methods by employing neutrosophy.

(a)   (b)
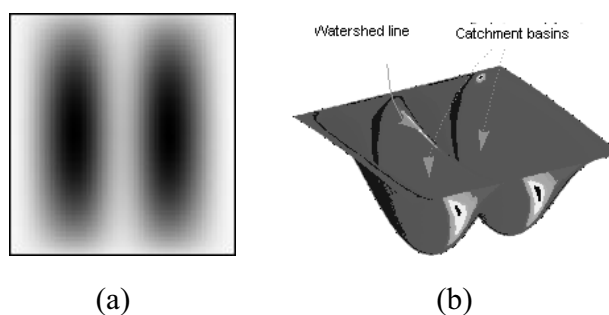
Figure 2.1. Watershed concept. (a) Two dark blobs. (b) 3D view of the watershed image of (a).

2.2 Proposed Method

Watershed image segmentation is good for handling a uniform background and objects with blurry edges. In this chapter, objects are defined as T and background as F. The blurry edges are gradually changed from objects to background, and there are no clear boundaries between the objects and edges or between the background and edges. The blurry boundaries are defined as I. Figure 2.2 is the flowchart of the proposed approach. An input image is mapped to T and F by the S-function. Two thresholds t_t
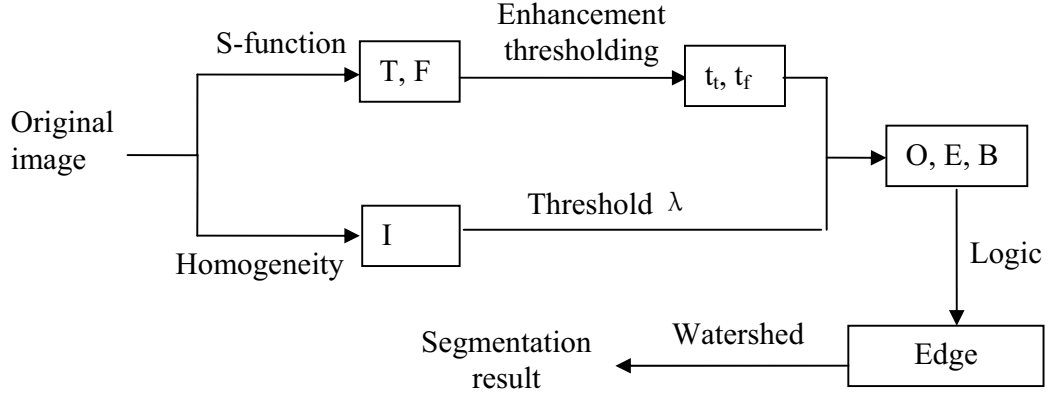
Figure 2.2. Flowchart of proposed method.

and t_f are decided in the enhanced T and F domains. The original image is also mapped

to indeterminacy domain I. The boundary regions are calculated by combining T, F and

I. The watershed method is applied to the boundary regions and finds connecting edges.

2.2.1 Map Image and Decide $\{T, F\}$

Given an image A, $P(x, y)$ is a pixel in the image, and (x, y) is the position of this

pixel. A 5x5 mean filter (the size of filter may vary depending on the size of input image)

is applied to A to remove noise and make the image uniform. Next, the image is

converted by using the S-function:

$$T(x,y) = S(g_{xy}, a, b, c) = \begin{cases} 0 & 0 \le g_{xy} \le a \\ \dfrac{(g_{xy} - a)^2}{(b-a)(c-a)} & a \le g_{xy} \le b \\ 1 - \dfrac{(g_{xy} - c)^2}{(c-b)(c-a)} & b \le g_{xy} \le c \\ 1 & g_{xy} \ge c \end{cases} \tag{0.1}$$

where g_{xy} is the intensity value of pixel $P(i, j)$. Variables a, b and c are the parameters that determine the shape of the S-function as shown in Figure 2.3.
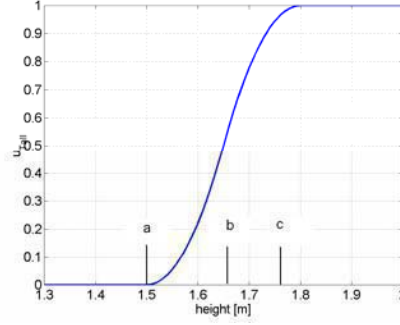
Figure 2.3. S-function.

Values of parameters a, b, and c can be calculated by using the simulated annealing method [40]. However, the simulated annealing algorithm is quite time consuming. Thus, we use another histogram-based method to calculate a, b, and c [41].

(1) Calculate the histogram of the image

(2) Find the local maxima of the histogram: $His_{\max}(g_1), His_{\max}(g_2), ...His_{\max}(g_n)$. Calculate the mean of local maxima:

$$\overline{His_{\max}(g)} = \frac{\sum_{i=1}^{n} His_{\max}(g_i)}{n} \tag{0.2}$$

(3) Find the peaks greater than $\overline{His_{\max}(g)}$, let the first peak be $g_{\min}$ and the last peak be $g_{\max}$

(4) Define low limit B_1 and high limit B_2:

$$\sum_{i=g_{\min}}^{B_1} His(i) = f_1$$

$$\sum_{i=B_2}^{g_{\max}} His(i) = f_1$$

(0.3)

where the information loss is allowed in the range $[g_{\min}, B_1]$ and $[B_2, g_{\max}]$, which is f_1

($f_1 = 0.01$ in the experiments).

(5) Determine a and c

$$a = (1 - f_2)(g_1 - g_{\min}) + g_{\min}$$
$$if\ (a > B_1) \qquad then \qquad a = B_1$$

(0.4)

$$c = f_2(g_{\max} - g_n) + g_n$$
$$if\ (c > B_2) \qquad then \qquad c = B_2$$

(0.5)

where $f_2 = 0.01$, and B_1 and B_2 are used to avoid important information loss. The

intensity less than B_1 is considered as background, and the intensity greater than B_2 is

considered as noise.

(6) Calculate parameter b by using the maximum entropy principal [42].

$$H(X) = \frac{1}{M \times N} \sum_{i=1}^{M} \sum_{j=1}^{N} S_n(T(x, y))$$

(0.6)

where $S_n()$ is a Shannon function defined as:

$$S_n(T(x, y)) = -T(x, y)\log_2 T(x, y) - (1 - T(x, y))\log_2(1 - T(x, y))$$
$$x = 1, 2, \cdots, M, y = 1, 2, \cdots N$$

(0.7)

The maximum entropy principle states that the greater the entropy is, the more

information the system includes [43-44]. To find the optimal b try every $b \in [a+1, c-1]$.

The optimal b will generate the largest $H(X)$:

$$H_{\max}\left(X,a,b_{opt},c\right)=\max\left\{H\left[X;a,b,c\right]|\,g_{\min}\le a<b<c\le g_{\max}\right\} \tag{0.8}$$

After a, b, and c are determined, the image can be mapped from the intensity domain g_{xy} to the new domain $T(x,y)$. Figure 2.4(a) is a cloud image. Figure 2.4 (b) is the result of (a) after mapping.

(a)   (b)
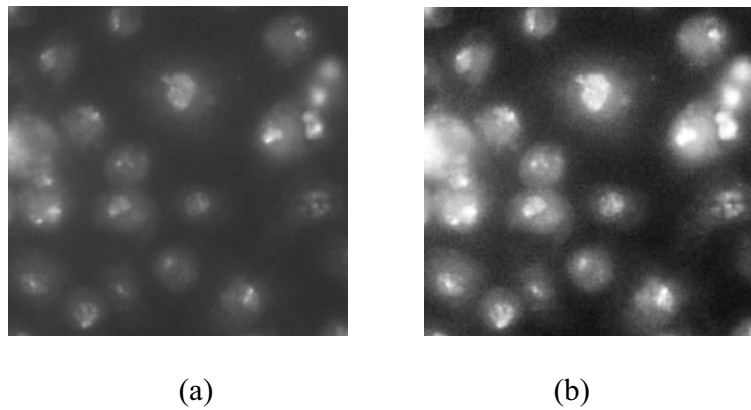
Figure 2.4. Cloud image. (a) Original image. (b) Result after applying the S-function.

2.2.2 Enhancement

Use intensification transformation to enhance the image in the new domain [45]:

$$\begin{aligned}
T_E &= E(T(x,y)) = 2T^2(x,y) & 0\le T(x,y)\le 0.5\\
T_E &= E(T(x,y)) = 1-2(1-T(x,y))^2 & 0.5<T(x,y)\le 1
\end{aligned} \tag{0.9}$$

$$F_E(x,y)=1-T_E(x,y) \tag{0.10}$$

Figure 2.5 is the result after enhancement.
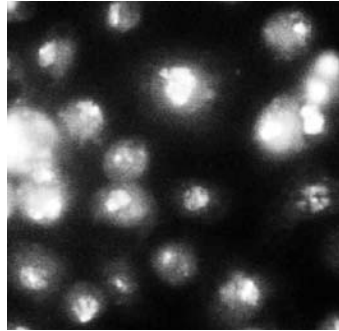
Figure 2.5. Result after enhancement.

2.2.3 Find Thresholds in T_E and F_E

Two thresholds are needed to separate the new domains T_E and F_E. A heuristic approach is used to find the thresholds in T_E and F_E [10].

(1) Select an initial threshold t_0 in T_E.

(2) Separate T_E by using t_0, and produce two new groups of pixels: T_1 and T_2, μ_1 and μ_2 are the mean values of these two parts, respectively.

(3) Compute the new threshold value: $t_1 = \dfrac{\mu_1 + \mu_2}{2}$

(4) Repeat steps 2 through 4 until the difference of $t_n - t_{n-1}$ is smaller than ε ($\varepsilon = 0.0001$ in the experiments) in the two successive iterations. Then, a threshold t_t is calculated. Figure 2.6(a) is the binary image generated by using t_t.

Applying the above steps in F_E domain, a threshold t_f can be calculated. Figure 2.6(b) is the resulting image by using t_f.

(a)   (b)
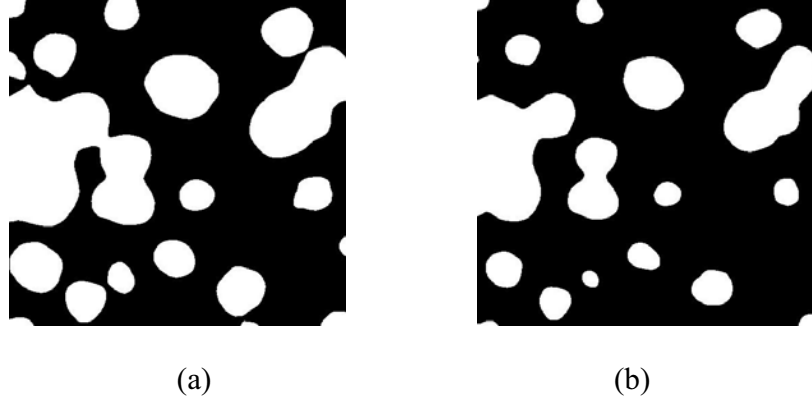
Figure 2.6. Result after applying t_t and t_f. (a) Image by applying threshold t_t. (b) Image by applying threshold t_f.

2.2.4 Define Homogeneity and Decide I

Homogeneity is related to local information, and plays an important role in image segmentation. I define homogeneity by using the standard deviation and discontinuity of the intensity. Standard deviation describes the contrast within a local region, while discontinuity represents the changes in gray levels. Objects and background are more uniform, and blurry edges are gradually changing from objects to background. The homogeneity value of objects and background is larger than that of the edges.

A size $d \times d$ window centered at (x, y) is used for computing the standard deviation of pixel $P(i, j)$:

$$sd(x, y) = \sqrt{\frac{\sum_{p=x-(d-1)/2}^{x+(d-1)/2} \sum_{q=y-(d-1)/2}^{y+(d-1)/2} (g_{pq} - \mu_{xy})^2}{d^2}} \qquad (0.11)$$

where μ_{xy} is the mean of the intensity values within the window.

$$\mu_{xy} = \frac{\displaystyle\sum_{p=x-(d-1)/2}^{x+(d-1)/2} \sum_{q=y-(d-1)/2}^{y+(d-1)/2} g_{pq}}{d^2}$$

The discontinuity of pixel $P(i, j)$ is described by the edge value. I use Sobel operator to calculate the discontinuity.

$$eg(x, y) = \sqrt{G_x^2 + G_y^2} \tag{0.12}$$

where G_x and G_y are the horizontal and vertical derivative approximations.

Normalize the standard deviation and discontinuity, and define the homogeneity as

$$H(x, y) = 1 - \frac{sd(x, y)}{sd_{max}} \times \frac{eg(x, y)}{eg_{max}} \tag{0.13}$$

where $sd_{max} = \max\{sd(x, y)\}$, and $eg_{max} = \max\{eg(x, y)\}$.

The indeterminate $I(x, y)$ is represented as

$$I(x, y) = 1 - H(x, y) \tag{0.14}$$

Figure 2.7 is the homogeneity image in domain I. The value of $I(x, y)$ has a range of $[0,1]$. The more uniform the region surrounding a pixel is, the smaller the indeterminate value of the pixel is. The window size should be big enough to include enough local information, but still be less than the distance between two objects. I chose d=7 for my experiments.
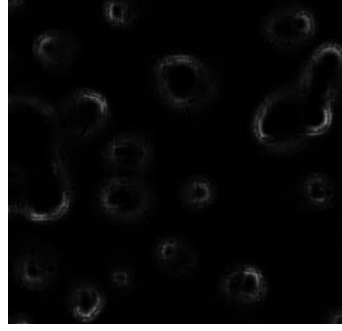
Figure 2.7. Homogeneity image in domain I.

2.2.5 Convert Image into Binary Image Based on $\{T_E, I, F_E\}$

In this step, a given image is divided into three parts: objects (O), edges (E), and background (B). $T(x, y)$ represents the degree of being an object pixel, $I(x, y)$ is the degree of being an edge pixel, and $F(x, y)$ is the degree of being a background pixel for pixel $P(x, y)$, respectively. The three parts are defined as follows:

$$O(x, y) = \begin{cases} true & T_E(x, y) \geq t_t, I(x, y) < \lambda \\ false & others \end{cases}$$

$$E(x, y) = \begin{cases} true & T_E(x, y) < t_t \vee F_E(x, y) < t_f, I(x, y) \geq \lambda \\ false & others \end{cases} \quad (0.15)$$

$$B(x, y) = \begin{cases} true & F_E(x, y) \geq t_f, I(x, y) < \lambda \\ false & others \end{cases}$$

where t_t and t_f are the thresholds computed in Subsection 2.2.3, and $\lambda = 0.01$.

After O, E, and B are determined, the image is mapped into a binary image for further processing. The objects and background are mapped to 0, and the edges are mapped to 1 in the binary image. The mapping function is as follows. See Figure 2.8.

$$Binary(x, y) = \begin{cases} 0 & O(x, y) \vee B(x, y) \vee \overline{E(x, y)} = true \\ 1 & others \end{cases} \quad (0.16)$$
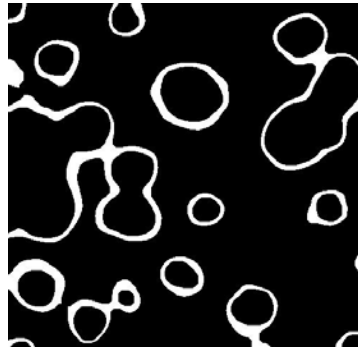
Figure 2.8. Binary image based on $\{T_E, I, F_E\}$.

2.2.6 Apply Watershed Algorithm

The watershed algorithm is good for finding optimal segmentation boundaries. The following is the watershed algorithm for the obtained binary image [46]:

(1)   Get regions $R_1, R_2, ..., R_n$, which represent the objects and background and have a value of 0. See Figure 2.9.

(2)   Dilate these regions by using a 3×3 structure element.

(3)   Build a dam at the place where the two regions get merged.

(4)   Repeat step (3) until all regions merge together. See Figure 2.10.

(a)   (b)   (c)   (d)
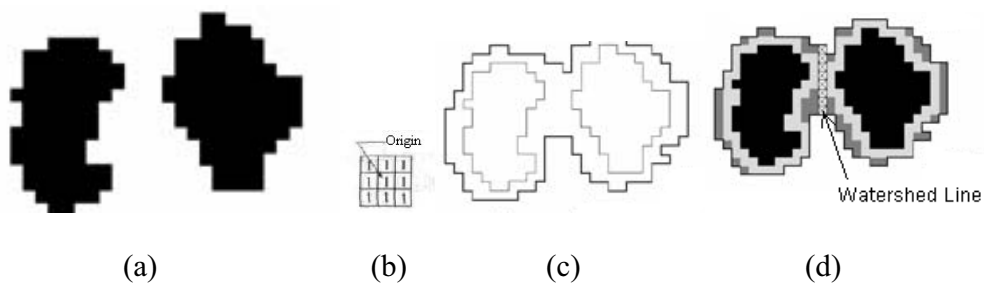
Figure 2.9. Watershed method. (a) Two regions that have value 0. (b) 3x3 structure element (c) Dilation of the two regions. (d) Dam construction.
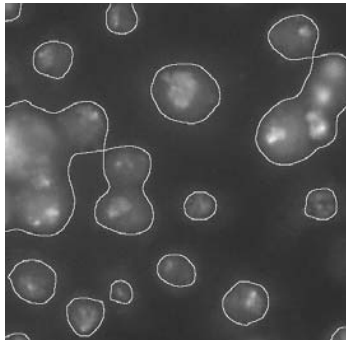
Figure 2.10. Final result after applying the proposed watershed method.

2.3 Experimental Results

Watershed segmentation is good for processing nearly uniform images; it can get a good segmentation, and the edges are connected very well. But this method is sensitive to noise and often has an over-segmentation problem [47]. I next compare my method with the pixel-based, edge-based, region-based and other two watershed methods.

Figure 2.11(a) is a cloud image that has blurry boundaries, and (b) is the result by using the pixel-based embedded confidence method [48], which determines the threshold value of a gradient image and consequently performs edge detection. The resulting image is under-segmented, and it only detects part of the boundaries. Figure 2.11(c) uses the Sobel operator which is an edge-based method. It, too, has under-segmentation, and the boundaries are not connected well. Figure 2.11(d) is the result by using the edge detection and image segmentation system (EDISON) [49] which applies a mean-shift region-based method [50]. In mean-shift-based segmentation, pixel clusters or image segments are identified with unique modes of the multi-modal probability density function by mapping each pixel to a mode using a convergent, iterative process. Three parameters in EDISON need to be manually selected: spatial bandwidth, color,

(a)　　　　　　　　　　(b)　　　　　　　　　　(c)

(d)　　　　　　　　　　(e)　　　　　　　　　　(f)

(g)
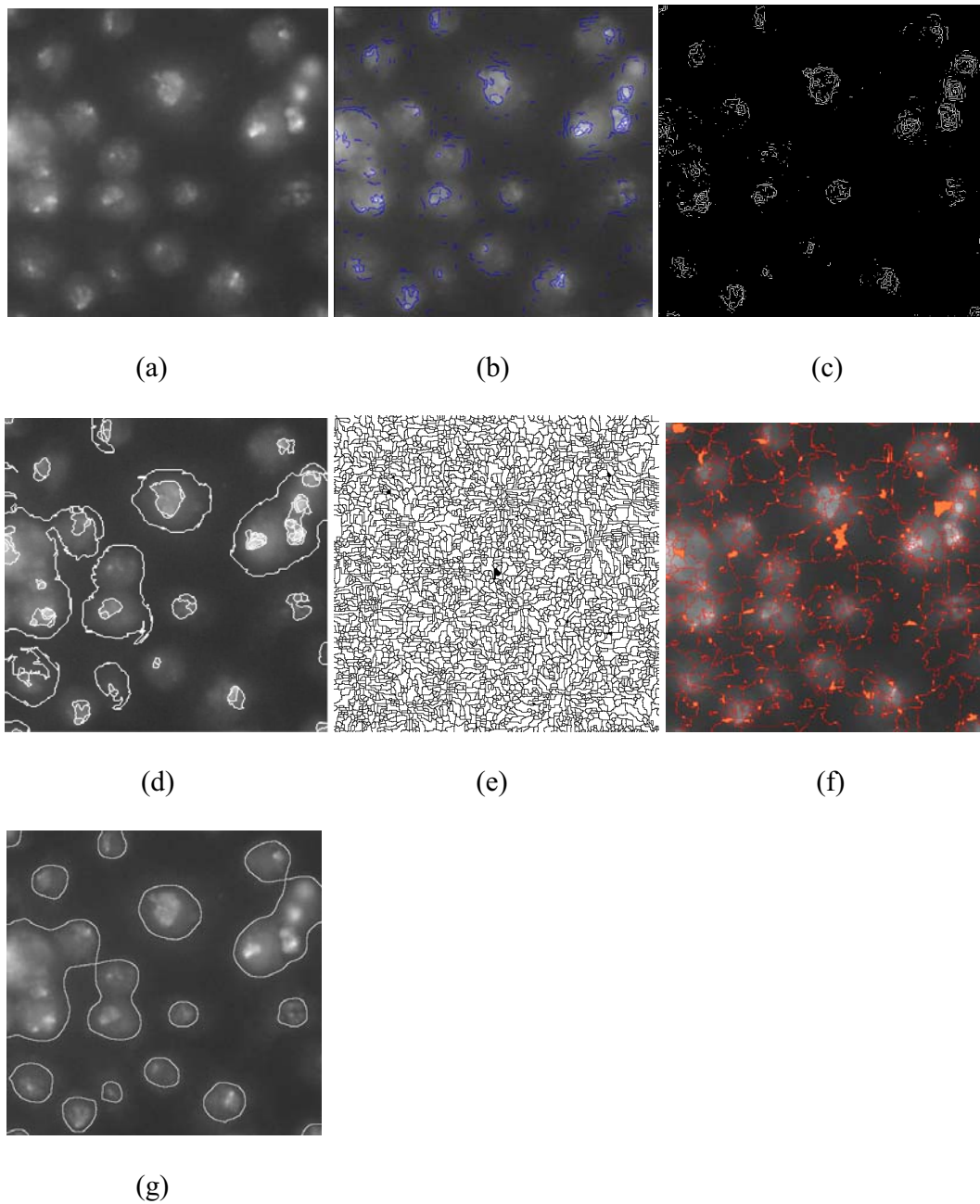
Figure 2.11. Cloud image. (a) Original image. (b) Result using the embedded confidence method. (c) Result using the Sobel operator. (d) Result using the mean-shift method. (e) Result using the watershed in Matlab. (f) Result using toboggan-based watershed. (g) Result using the proposed method.

and minimum region. I tried different combinations of these parameters and got the best result, as shown in Figure 2.11(d) (spatial bandwidth = 6, color = 3, minimum = 50). The edges in (d) are well connected but not smooth, the result is over-segmented. Figure 2.11(e) utilizes the watershed method in Matlab, and the result shows heavy over-segmentation, making it hard to find distinguishable objects. Figure 2.11(f) is the result from a modified watershed method (toboggan-based method) [51]. It can efficiently group the local minima by assigning them a unique label. The result is better than (e), but the background and objects are still mixed together. Figure 2.11(g) applies the proposed method, and it gets clear and well connected boundaries. The result gives an improvement better than those obtained by other methods used in (b), (c), (d), (e), and (f).

Figure 2.12(a) is a blurry cells image. The objects and boundaries are not clear. The edges detected by the embedded confidence method in (b) are discontinued. The Sobel operator in (c) almost loses all boundaries. The mean-shift method in (d) (spatial bandwidth= 7, color = 3, minimum = 10) produces few connected edges, and the edges are not well detected. Two watershed methods in (e) and (f) produce over-segmentation. The result in (g) using the proposed method has well connected and clear boundaries to segment the cells from the background better.

One drawback of watershed methods is noise sensitivity. However, the proposed method is very noise-tolerant. Figure 2.13(a) is a noise-free coin image, and (b), (c), and (d) are the results from employing the watershed method in Matlab, toboggan-based watershed method, and the proposed neutrosophic watershed method, respectively.

(a)   (b)   (c)

(d)   (e)   (f)

(g)
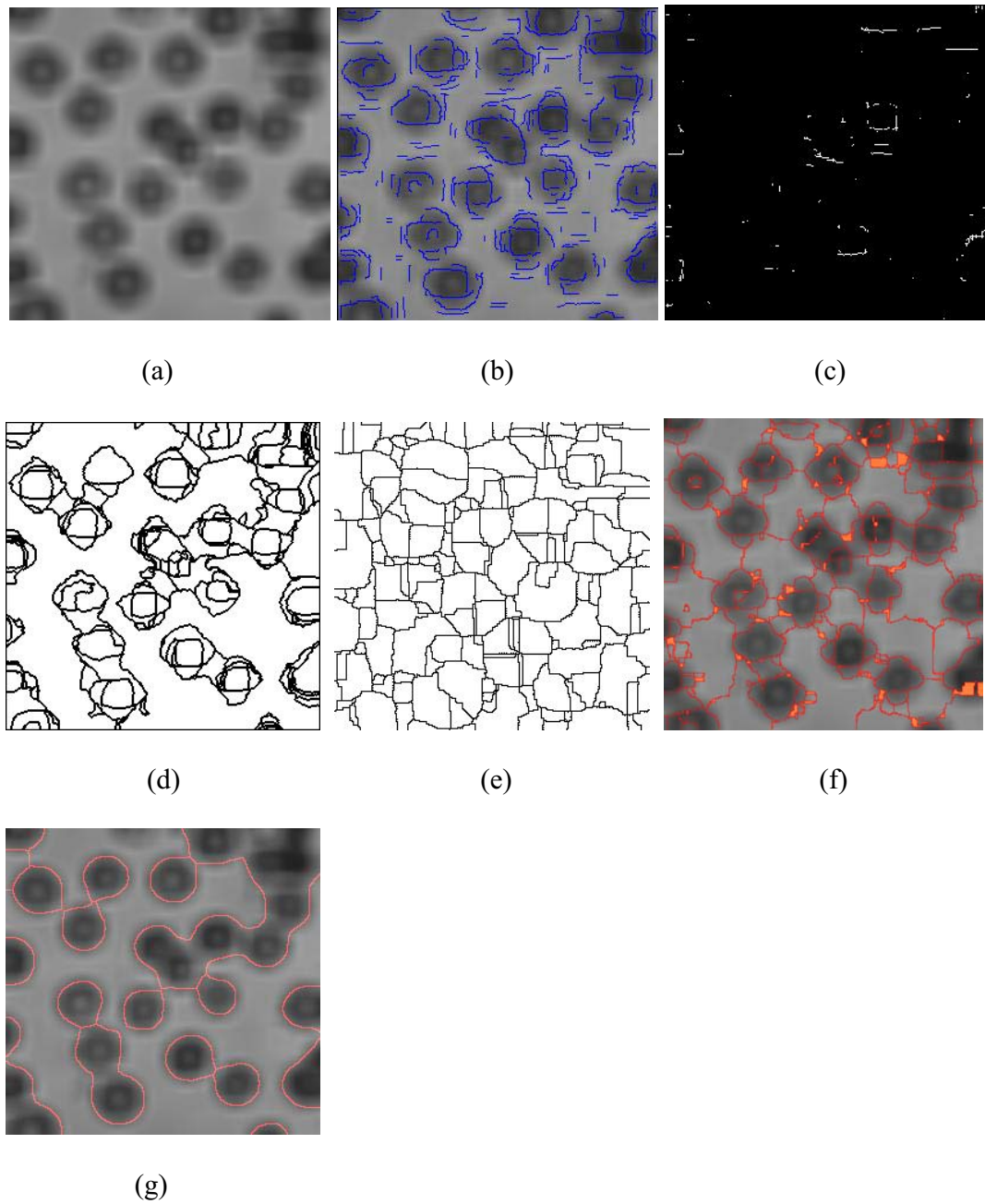
Figure 2.12. Cell image. (a) Blurry cell image. (b) Result using the embedded confidence edge detector. (c) Result using the Sobel operator. (d) Result using the mean-shift method. (e) Result using the watershed in Matlab. (f) Result using the toboggan-based watershed. (g) Result using the proposed method.

(a)　　　　　　　(b)　　　　　　　(c)

(d)　　　　　　　(e)　　　　　　　(f)

(g)　　　　　　　(h)
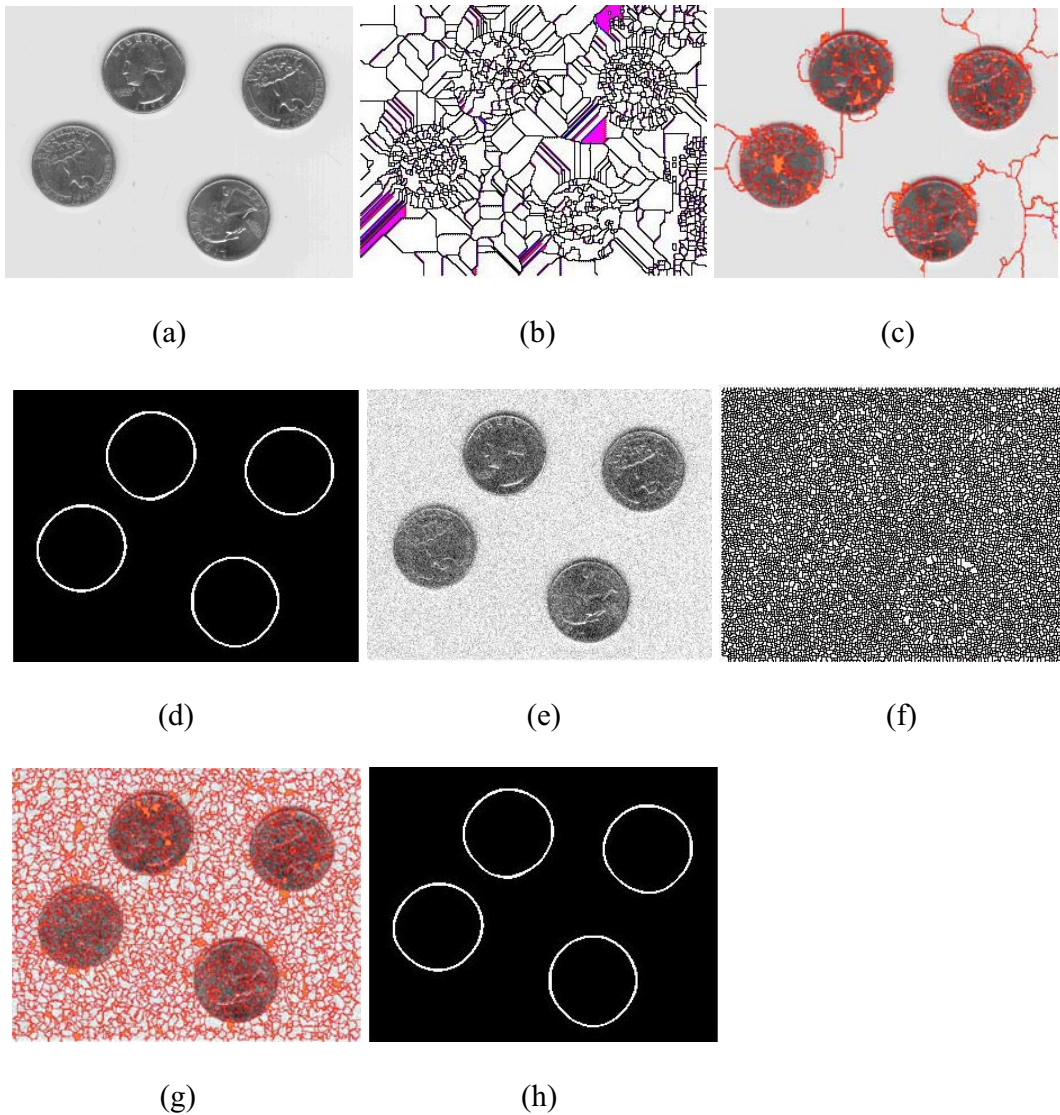
Figure 2.13. Coin image. (a) Original image. (b) Result using the watershed in Matlab on the original image. (c) Result using the toboggan-based watershed on the original image. (d) Result using the proposed method on the original image. (e) Image with Gaussian noise added. (f) Result using the watershed in Matlab on the noisy image. (g) Result using the toboggan-based watershed on the noisy image. (h) Result using the proposed method on the noisy image.

Figure 2.13(e) is the image after adding Gaussian noise (mean is 0, and standard variance is 2.55) to (a). Figure 2.13(f), (g), and (h) are the results from applying the above three watershed methods to (e). We can see that the Gaussian noise has a big impact on the results of the existing watershed methods, and causes heavy over-segmentation. But the proposed neutrosophic watershed method is quite noise-tolerant.

Another problem of existing watershed algorithms is that they do not work well for non-uniform images. In Figure 2.14(a), the capitol has a wide range of intensities. The top of the capitol is dark, the middle part of the capitol is gray, and the bottom part of capitol is white. Figure 2.14(b) is the result of applying the watershed method in Matlab, and (c) is the result of applying the toboggan-based watershed method. Neither works well. Figure 2.14(d) is the result of applying the proposed method. As shown, the capitol is segmented well.

2.4 Conclusions

In this chapter, neutrosophy is employed in gray level images, and a novel watershed image segmentation approach based on neutrosophic logic is introduced. In the first phase, a given image is mapped to three subsets T, F and I, which are defined in different domains. Thresholding and neutrosophic logic are employed to obtain a binary image. Finally, the proposed watershed method is applied to get the segmentation result. I compare my method with pixel-based, edge-based, region-based segmentation methods, and two existing watershed methods. The experiments show that the proposed method has better performance on noisy and non-uniform images than that obtained by

using other watershed methods, since the proposed approach can handle uncertainty and

indeterminacy better.

(a)   (b)

(c)   (d)
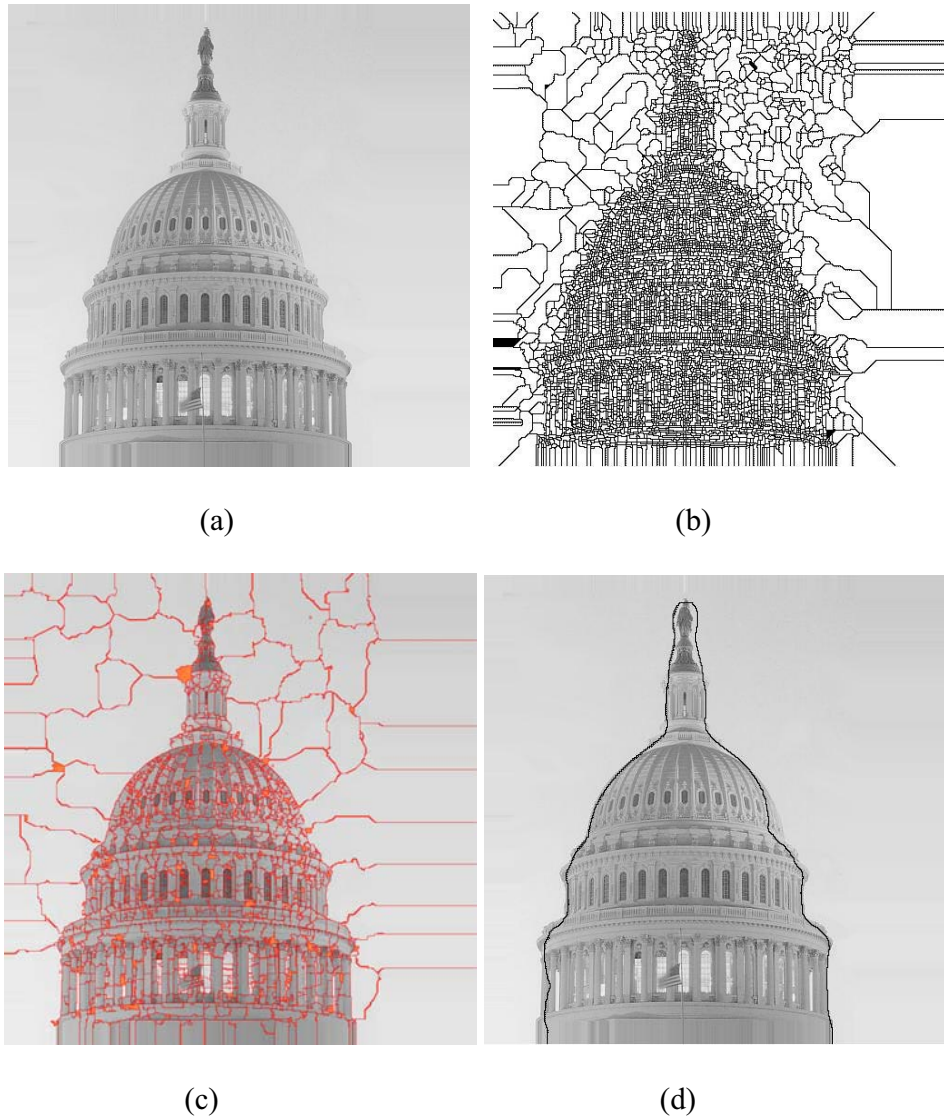
Figure 2.14. Capitol image. (a) Original capitol image. (b) Result using the watershed in Matlab. (c) Result using the toboggan-based method. (d) Result using the proposed method.

CHAPTER 3

BREAST ULTRASOUND IMAGE SEGMENTATION

BASED ON NEUTROSOPHY

3.1 Introduction

Cancer is one of the dangerous diseases for humans. One out of eight deaths in the world is caused by cancer [52]. It is the second leading cause of death in developed countries and the third leading cause of death in developing countries. According to [53], in 2009, 562,340 Americans, 1,500 people a day, died of cancer. Approximately 1,479,350 new cancer cases were diagnosed in the United States in 2009.

Breast cancer is the most commonly diagnosed cancer among women and is the second leading death cause of women in the United States [54]. A total 209,060 new breast cancer cases and 40,230 deaths are projected to occur in 2010 [55]. Although breast cancer has a high death rate, the cause of breast cancer is still unknown [56]. Early detection is a critical step towards treating breast cancer and plays a key role in diagnosis.

There are three major types of diagnostic techniques used by radiologists to detect breast cancer: mammography [57-58], ultrasound, and magnetic resonance imaging (MRI).

While mammography is the most frequently used of these techniques, it has some disadvantages:

1. It is not always accurate in detecting breast cancer [59]. Approximately 65% of cases referred to surgical biopsy are actually benign lesions [60-61].

2. Mammography has limitations in cancer detection in the dense breast tissue of young patients. The breast tissue of young women tends to be dense and full of milk glands. Most cancers arise in dense tissue, and it is challenging for mammography to detect lesion in this higher risk category.

3. In mammograms, glandular tissues look dense and white, much like cancerous tumors [62].

4. Mammography may identify an abnormality that looks like a cancer, but turns out to be normal. Thus, additional tests and diagnostic procedures are often required. It is a stressful procedure for patients. To make up for these limitations, sound diagnosis is often needed in addition to mammography [63].

5. Reading mammograms is a demanding job for radiologists. An accurate diagnosis depends on training, experience, and other subjective criteria. Around 10 percent of breast cancers are missed by radiologists, and most of them are in dense breasts [64]. And about two-thirds of the lesions that are sent for biopsy are benign. The reasons for this high miss rate and low specificity in mammography are the following: the low conspicuity of mammographic lesions, the noisy nature of the images, and the overlying and underlying structures that obscure features of a region of interest (ROI) [65].

Ultrasound techniques use high frequency broadband sound waves in the megahertz range. These waves are reflected by tissue to varying degrees to produce images. An ultrasound image is a gray level display of the area being imaged and is used in imaging abdominal organs, heart, breast, muscles, tendons, arteries and veins. An ultrasound

allows for studying the function of moving structures in real-time and has no ionizing radiation. It is relatively cheap and quick to perform. Since an ultrasound is noninvasive, practically harmless, and cost effective for diagnosis, it has become one of the most prevalent and effective medical imaging technologies. In breast cancer detection, it is an important adjunct to mammography and has following advantages:

1. Use of ultrasounds in breast cancer detection has improved the true positive detection rate, especially for women with dense breasts [66-67]. According to [68], an ultrasound is more effective for women younger than 35. It has proven to be an important adjunct to mammography in breast cancer detection and useful for differentiating cysts from solid tumors.

2. It has been shown that ultrasound is superior to mammography in its ability to detect local abnormalities in the dense breasts of adolescent women [69]. The authors of [70] suggest that the denser the breast parenchyma, the higher the detection accuracy of malignant tumors using ultrasound. The accuracy rate of breast ultrasound (BUS) has been reported to be 96-100% in the diagnosis of simple benign cysts [71].

3. An ultrasound can obtain any section image of breast, and observe the breast tissues in real-time and dynamically.

4. Ultrasound devices are portable and relatively cheap, and they have no radiation and side effects.

However, ultrasound imaging has some limitations. It is low contrast, low resolution with speckle noise and blurry edges between different organs. These

characteristics make it is more difficult for radiologists to read and interpret ultrasound images. Table 3.1 lists the accuracy rate of doctors.

Table 3.1. Accuracy Rate of BUS Examination.

Type	Accuracy
Benign hyperplasia	84.5%
Benign tumor	79%
Malignant tumor	88.5%

Computer-aided detection (CAD) systems have been developed to help radiologists to evaluate medical images and detect lesions at an early stage [72]. They assist doctors in the interpretation of medical images. A typical CAD system in breast ultrasound helps radiologists evaluate ultrasound images and detect breast cancer. A breast ultrasound CAD system improves the ultrasound image quality, increases the image contrast, and automatically determines lesion. It also reduces the human workload. Figure 3.1 gives the general steps of an ultrasound CAD system.

Input Image

Image Preprocessing

Image Segmentation
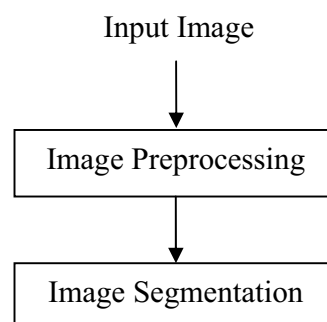
Figure 3.1. Breast ultrasound CAD system.

Breast ultrasound (BUS) images are low contrast and have speckles, thus making the segmentation of BUS images one of the most difficult steps in computer-aided diagnosis (CAD) algorithms. There is a controversy between two opinions about speckle in BUS images. (1) Speckle blurs a BUS image, and it is treated as noise to be removed [73-74]. (2) Speckle reflects the local echogenity of the underlying scatters and has certain useful pattern elements [75]. Most of the existing CAD systems are based on one of the above two opinions about speckle. Another problem in most of the existing BUS segmentation methods is that the algorithms are only applied to a restricted area, a region of interest (ROI), rather than the entire BUS image. The ROIs contain tumors [76-77], and they are manually or semi-automatically segmented [78]. There are four types of methods used for BUS image segmentation: edge-based methods [79-80], region-based methods [81-82], model-based methods [83], and neural network/Markov methods [84-86].

A BUS image is noisy and blurry due to artifacts, such as speckle, reverberation echo, acoustic shadowing, and refraction [87]. The boundaries of the tumors are unclear and hard to distinguish. In this paper, I define a tumor as <A>, the boundaries of the tumor as <Neut-A>, and the background as <Anti-A>. T, I, and F are the neutrosophic components to represent <A>, <Neut-A>, and <Anti-A>. <A> and <Anti-A> contain region information, while <Neut-A> has boundary information.

A pixel of an image in the neutrosophic domain can be represented as $A\{t, i, f\}$, meaning the pixel is $t\%$ true (tumor), $i\%$ indeterminate (tumor boundaries), and $f\%$ false (background), where $t \in T$, $i \in I$, and $f \in F$, and T, I and F represent true,

indeterminacy and false domains, respectively. In the classical set, $i = 0$, t and f are either 0 or 100. In the fuzzy set, $i = 0$, $0 \leq t, f \leq 100$. In the neutrosophic set, $0 \leq t, i, f \leq 100$.

3.2 Tumor Detection Method

Because a BUS is blurred image, I can use the algorithm presented in Chapter 2 to find the boundaries of a tumor. However, because BUS images contain speckles, reverberation echoes, and acoustic shadow artifacts, the segmentation result may include non-tumor area. I remove such areas by utilizing the following rules:

(1) Remove the lines connected to the image boundaries.

(2) Remove the segmentation area whose size is less than one-third of the largest segmented area.

(3) Remove the segmentation area whose mean gray level is greater than the average gray level of the entire image.

(4) Remove the area whose ratio of width/length is equal to or greater than 4, since the shape of the tumor should be roundish or elliptical.

Figure 3.2 is the flowchart of BUS detection based on neutrosophy. Since the watershed method shrinks the segmented area, I use the boundary produced in Subsection 2.2.5 as the tumor boundary. Figure 3.3 is the resulting images of each step.
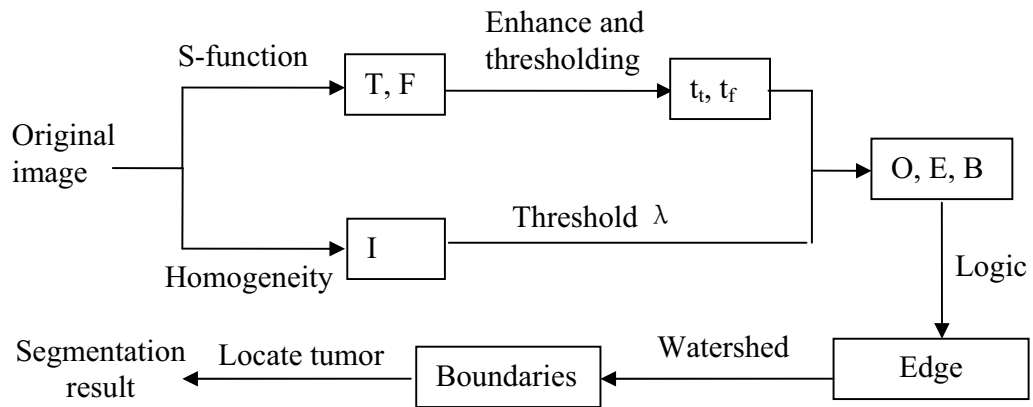
Figure 3.2. Flowchart of BUS detection.
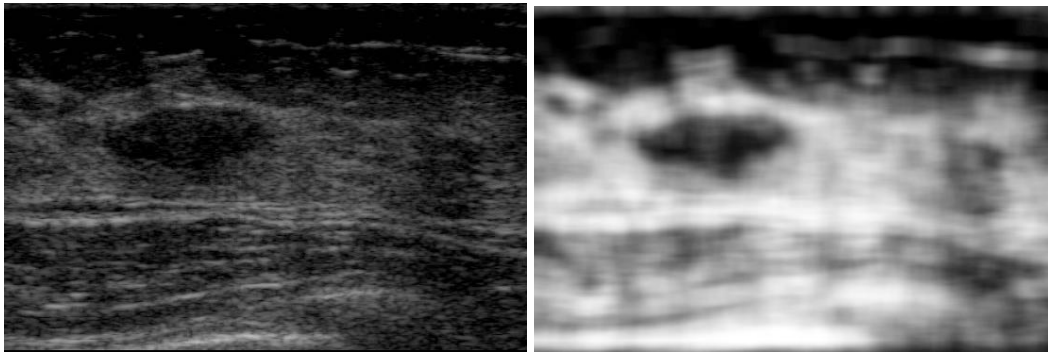
(a)   (b)

Figure 3.3. Resulting image of each step. (Continued on next page)

(c)

(d)

(e)

(f)

(g)
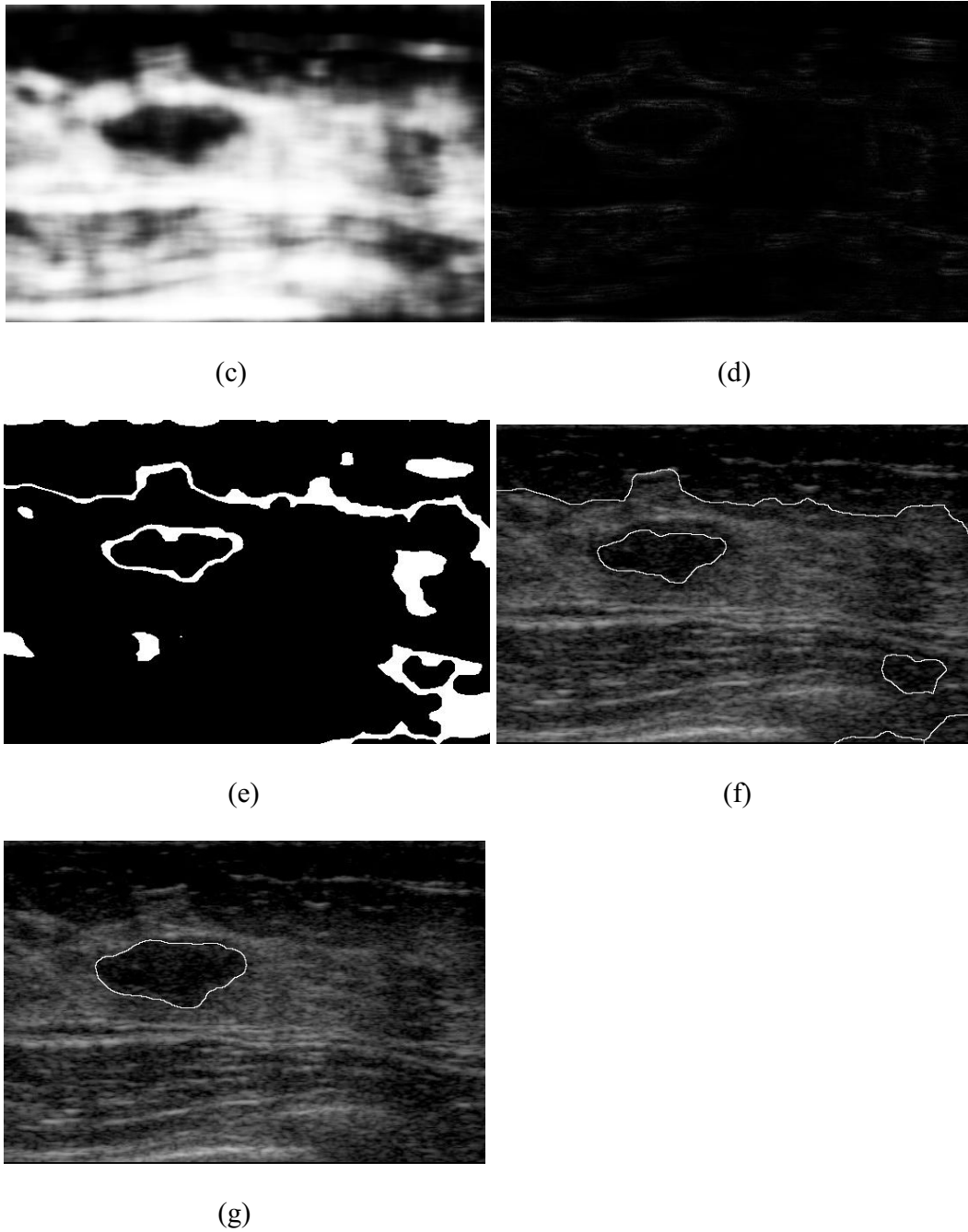
(Continued from previous page) Figure 3.3. Resulting image of each step. (a) BUS image. (b) Result after applying the S-function. (c) Result after enhancement. (d) Homogeneity image in domain I. (e) Redefined edges in neutrosophic domain. (f) Result after applying the watershed method. (g) Final result of the proposed segmentation method.

3.3 Experimental Results

My approach has the following advantages: it is noise-tolerant, fully automatic, and able to process low-contrast BUS images with high accuracy. The database used in my experiments contains 110 images (53 malignant, 37 benign, and 20 normal). Each image has only one tumor. The average size of image in the database is 370x450 pixels, with the largest being 470x560 pixels and the smallest 260x330 pixels. The images were collected by VIVID 7 with a 5-14 MHz linear probe. I used 10 images (5 malignant and 5 benign), in which were included the largest and smallest tumors, to determine the parameters of the algorithm.

3.3.1 Speckle Problem

As stated previously, there are two controversial opinions about speckle in BUS images: speckle is noise versus speckle is pattern. My method solves this controversy by combining these two opinions through use of neutrosophy. In T or F, the speckle is treated as noise. In I, the speckle is employed as a pattern for computing homogeneity. In Chapter 2, I demonstrate the noise-tolerance of the proposed algorithm in Figure 2.13 by adding Gaussian noise to (a).

3.3.2 Fully Automatic Method

One of the more difficult problems in BUS image segmentation is to find the tumor automatically. Many existing methods need to manually select a region containing the tumor as the initialization of segmentation. Often, the final segmentation depends on region selection. The geodesic active contour (GAC) model is an edge-based model [88]. Figure 3.4(b) is the segmentation result by applying the GAC model to the entire BUS

image of Figure 3.4(a). There is a manually selected ROI in Figure 3.4(c). However, applying the GAC model to Figure 3.4(c) is not enough to detect the tumor boundaries correctly. Figure 3.4(e) shows a more accurate, manually selected ROI. Figure 3.4(f) is the segmentation result of applying the GAC model to Figure 3.4(e), The results are still quite poor.

3.3.3 Low Contrast Images

Figure 3.5 shows some examples of low contrast BUS images and the segmentation results produced by the proposed approach. Figure 3.5(a) has reverberation echoes on the top and bottom caused by the ultrasound beam bouncing back and forth, with the aggregations of small and highly reflecting particles. Another difficulty is that the tumor has an acoustic shadow. There are intensely echogenic lines appearing at the surface of the structures which block the passage of the sound waves. Figure 3.5(c) is a much brighter image. Figure 3.5(e) has a dark area on the left side of the image caused by pointing the probe to the air accidently. Figure 3.5(b), (d), and (f) are the segmentation results of utilizing the proposed approach. They demonstrate that the proposed method can solve such problems very well.

3.3.4 Quantitative Evaluation

Because to date there is no a universally accepted objective standard for evaluating the performance of segmentation algorithms, manual delineations produced by radiologists are often used to evaluate the accuracy of BUS image segmentation [78, 82]. Because radiologists have different experience and skills, delineation results may vary [89]. Figure 3.6(b) is the segmentation result by a radiologist, and Figure 3.6(c) is the

result generated after the discussion of a group of radiologists. Figure 3.6(d) is the result by using the proposed approach.

Figure 3.7(a), (c) and (e) are the manual segmentation results by a group of radiologists. Figure 3.7(b), (d) and (e) are the results by the proposed algorithm. We can see that the proposed approach can outline the tumor shape very well, which is one of the most important features for CAD systems [90].

An active contour (AC) model is a region-based segmentation method [91-93]. It utilizes the means of different regions to segment a BUS image. Because AC requires manually selecting an ROI, I use a rectangular ROI that contains a tumor. The length and width of an ROI region are 2 times the length and width of the tumor. Figure 3.8(b) is the result by applying an AC model with 200 iterations to Figure 3.8(a). The result shows over-segmentation. Figure 3.8(c) is the result after removing the non-tumor region. However, the AC model does not work well on some BUS images (see Figure 3.8(e)).

In their recently published paper, the authors of [94] employ a fully automatic segmentation method on BUS images based on texture analysis and active contour (TE). It first divides the entire image into lattices of the same size, and then generates the ROI based on the texture information. Figure 3.9(b) is the result of applying the method in [94]. But this method will not work well on low contrast images (reverberation echoes, refraction, etc). Figure 3.9(d) segments a part of the background as a part of the tumor. Figure 3.9(f) locates the wrong ROI region.
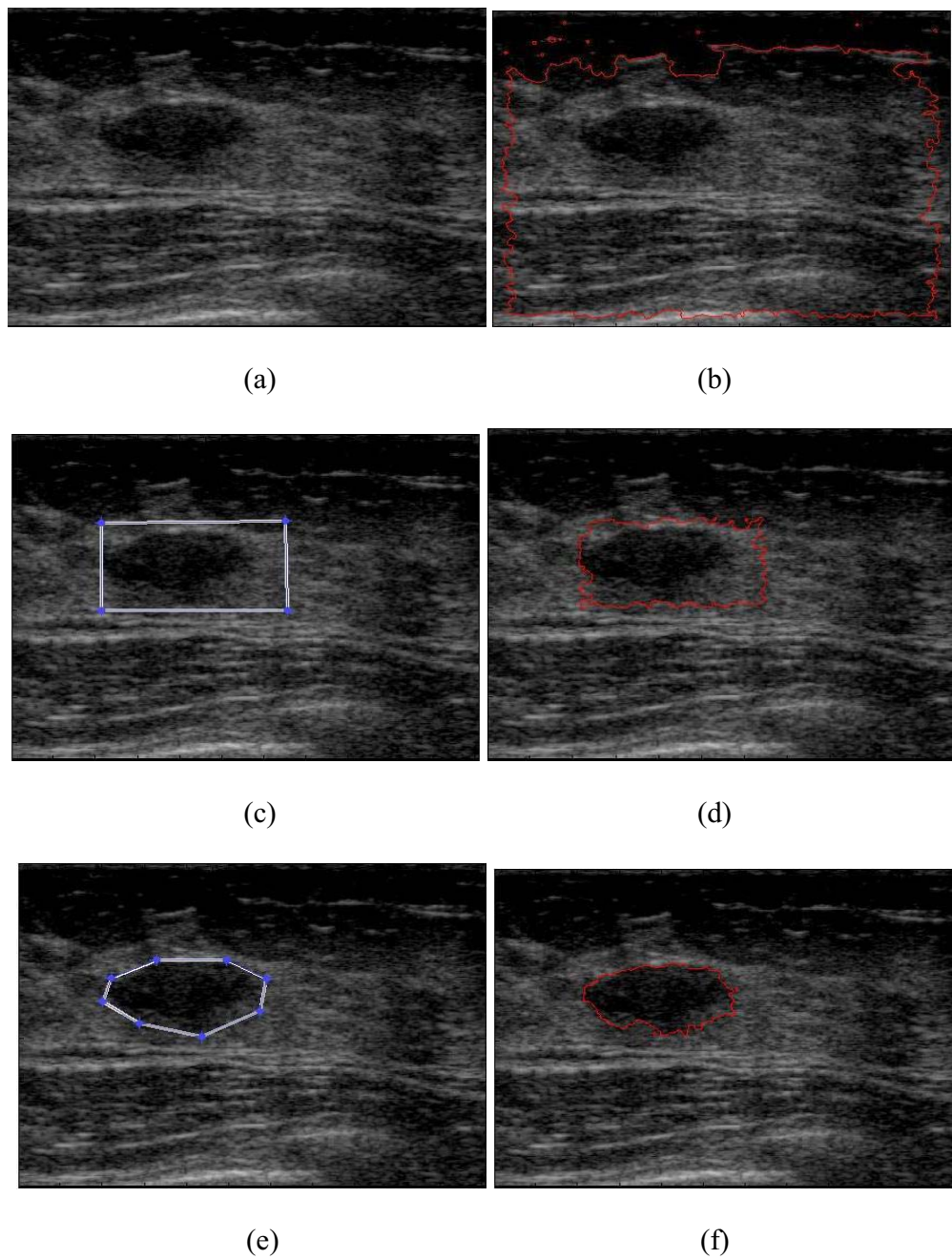
Figure 3.4. Result of GAC method. (a) BUS image. (b) The segmentation result by applying GAC model to (a). (c) Manually selected ROI. (d) The segmentation result by applying GAC Model to (c). (e) More accurately and manually selected ROI. (f) The segmentation result by applying GAC Model to (e).
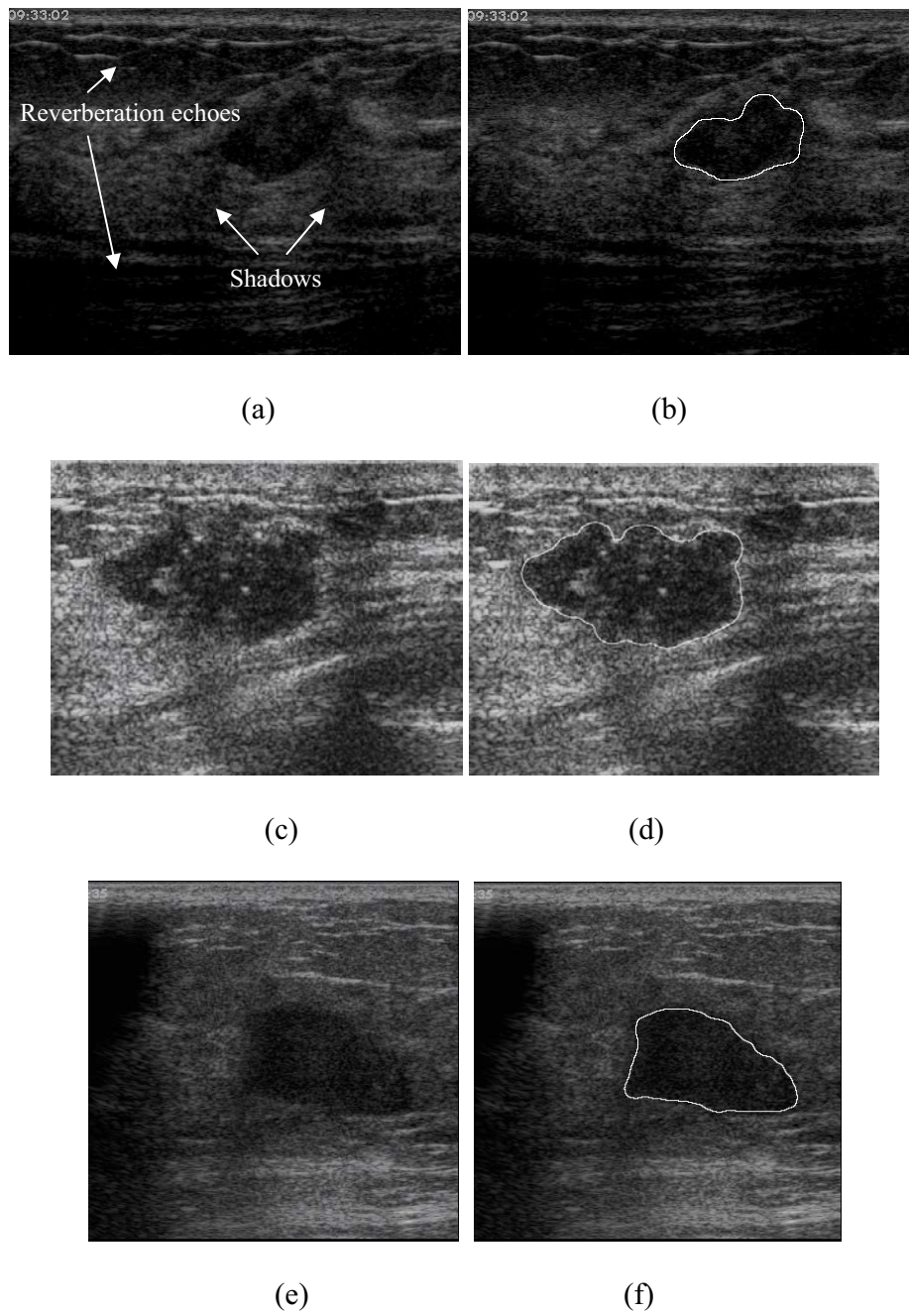
Figure 3.5. Low quality images. (a) BUS image with reverberation echo and shadow. (b) Result using the proposed method. (c) Bright BUS image. (d) Result using the proposed method. (e) BUS image with dark area on the left side. (f) Result using the proposed method.
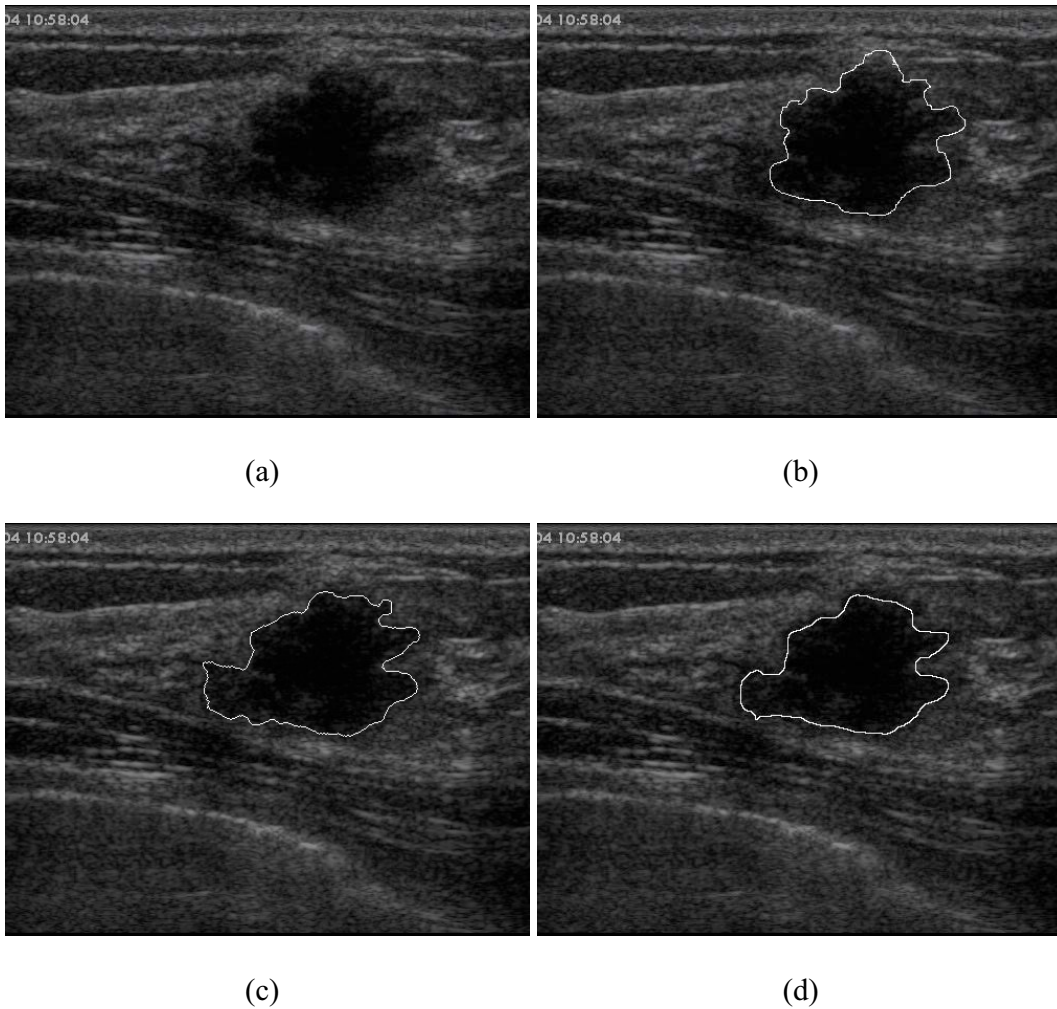
Figure 3.6. Comparison with manual outlines. (a) BUS image. (b) Manual segmentation result by a radiologist. (c) Manual segmentation result by a group of radiologists. (d) Result by using the proposed method.
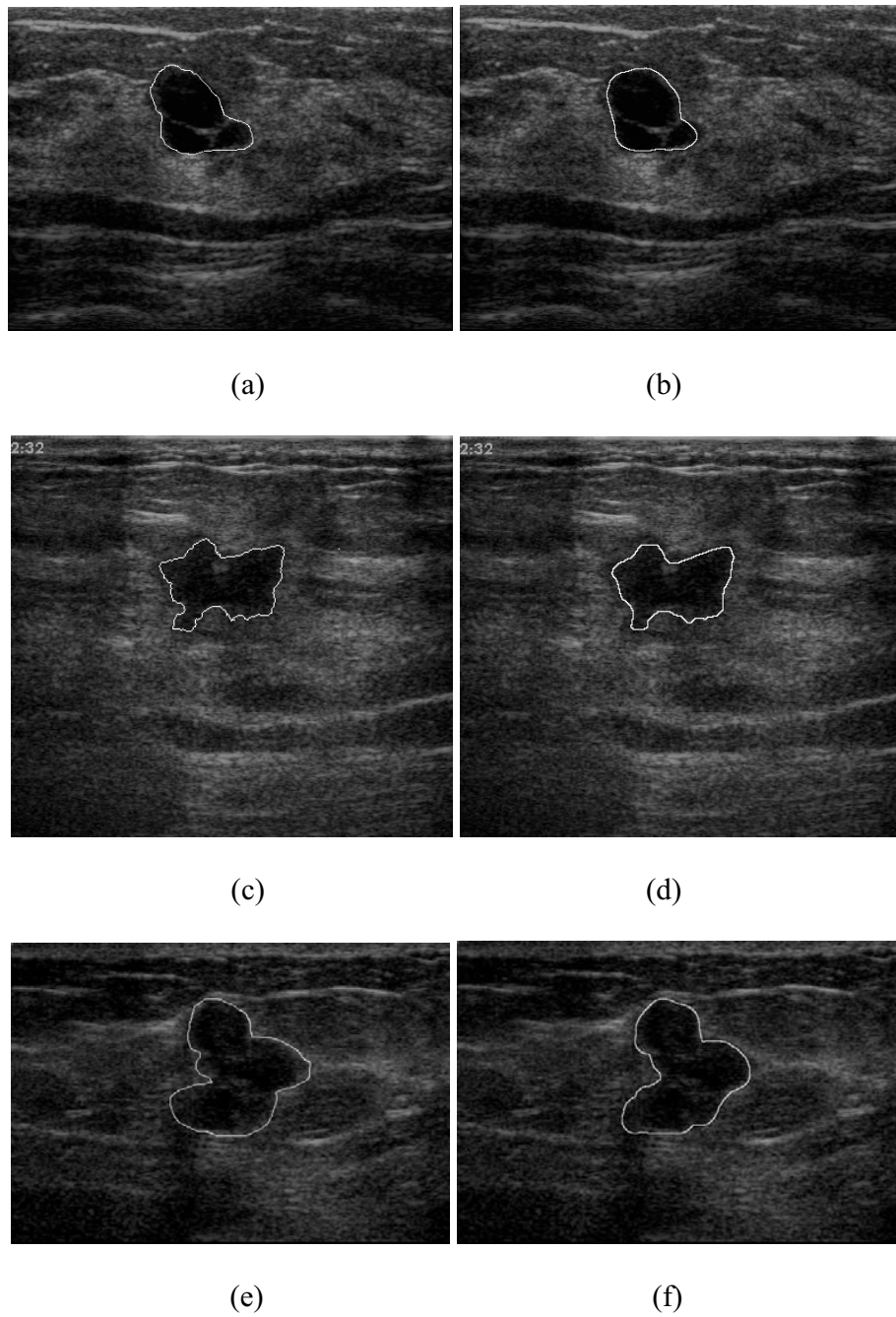
Figure 3.7. Result of proposed method. (a), (c) and (e) Manual segmentation results by a group of radiologists. (b), (d), and (f) Results by using the proposed algorithm.

(a) (b) (c)

(d) (e)
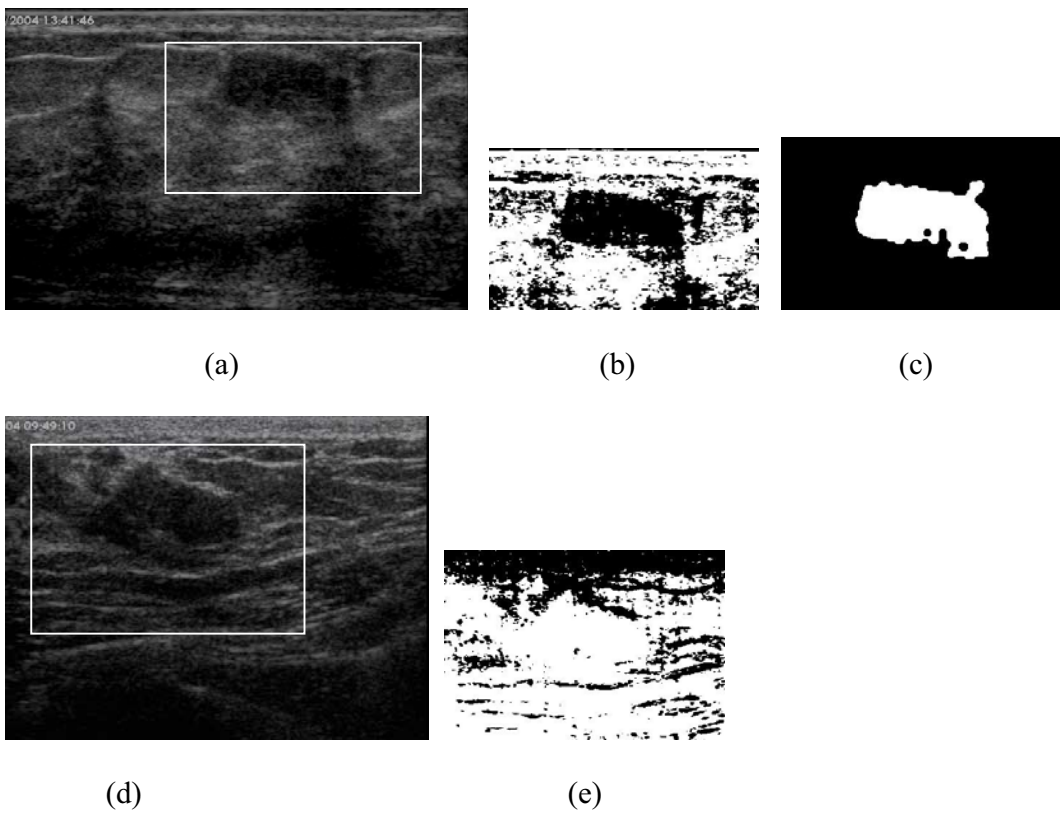
Figure 3.8. Result of AC method. (a) BUS images with manually selected ROI.
(b) Results by applying active contour method. (c) Result by removing non-tumor areas.
(d) BUS images with manually selected ROI. (e) Results by applying active contour
method.

(a)   (b)

(c)   (d)

(e)   (f)
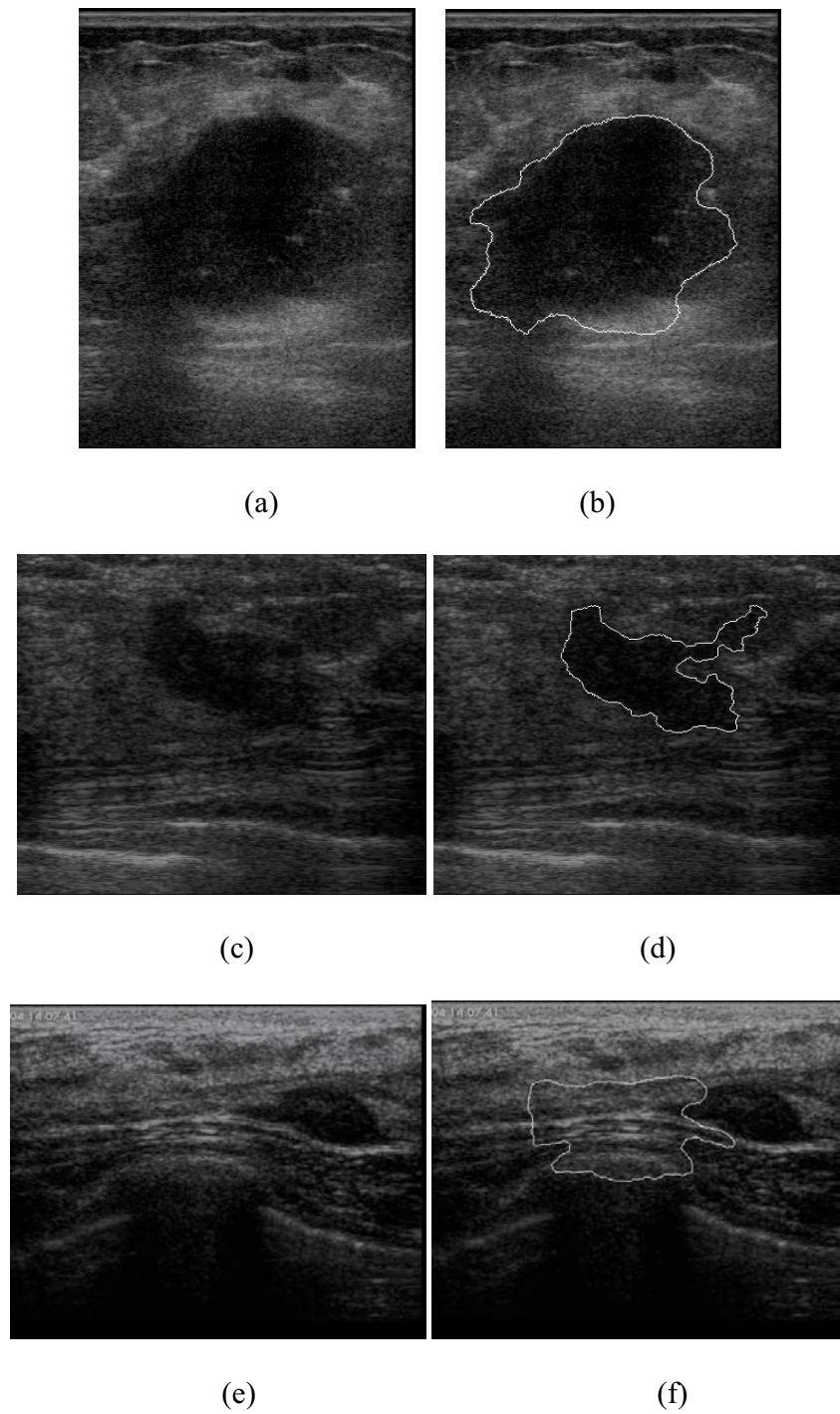
Figure 3.9. Result of TE method. (a), (c) and (e) BUS images. (b), (d) and (e) Result by applying the TE method in [95].

In this paper, I tested my method using 90 clinical images and used three area error metrics [96] for evaluating accuracy: true positive ratio (TP), false positive ratio (FP), and similarity (SI) defined as:

$$TP(\%) = \frac{|A_m \cap A_n|}{A_m}$$

$$FP(\%) = \frac{|A_m \cup A_n - A_n|}{A_m} \tag{1.1}$$

$$SI(\%) = \frac{|A_m \cap A_n|}{|A_m \cup A_n|}$$

where A_m refers to the tumor area determined by a group of radiologists and A_n is the area determined by the proposed algorithm, see Figure 3.10.
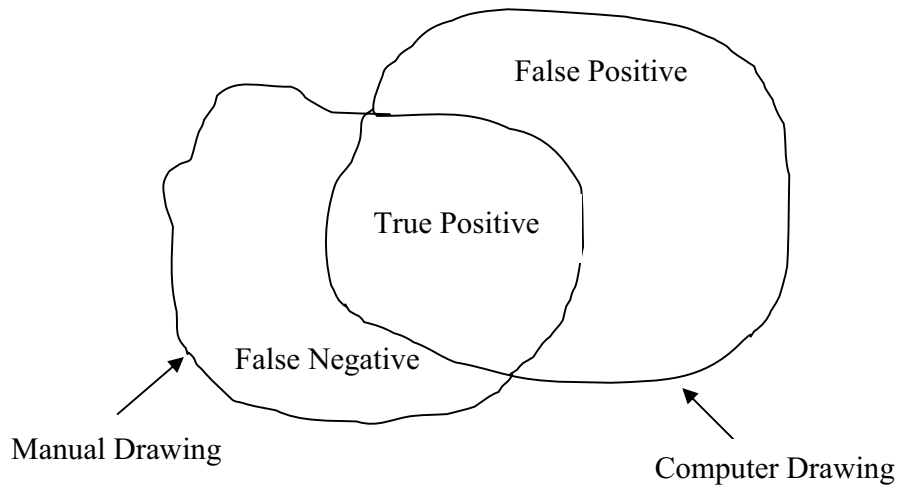
Figure 3.10. Areas corresponding to TP, FP, and FN.

In Table 3.2, active contour (AC) method, texture-based method (TE), and the proposed method are compared with the delineated results by the group of radiologists.

Table 3.2. Average Area Error Metrics.

	Malignant			Benign			Total		
	TP	FP	Similarity	TP	FP	Similarity	TP	FP	Similarity
AC[1]	64.1%	5.3%	63.7%	71.5%	6.8%	66.8%	67.4%	5.98%	65.1%
TE[2]	81.2%	38.3%	51.1%	84.2%	44.5%	47.8%	82.9%	41.2%	49.1%
Proposed method[3]	85.4%	11.7%	77.6%	89.6%	14.3%	78.3%	87.8%	13.3%	77.9%

[1] The inputs of active contour method are the manually selected ROIs. There are 40 out of 90 images in which the tumors can be located.
[2] The inputs of texture-based method are the entire BUS images. There are 62 out of 90 images in which the tumors can be located.
[3] The inputs of proposed method are entire BUS images. There are 84 out of 90 images in which the tumors can be located.

The source code of active contour is obtained from an introduction website of the AC method, which is based on [91]. It includes the application to medical image segmentation. In an active contour method, the input is a manually selected ROI. There are only 40 results for locating a tumor properly (90 images in the database). The accuracy of AC is calculated based on these 40 images. We can see that the TP (67.4% in total) of the AC method is very low even using ROIs only.

The inputs of TE and the proposed method are the entire BUS images, because both of them are designed as fully automatic methods. TE has 62 results correctly locating the tumors and the proposed method has 84. But, the false positive rate of TE is 41.2% which is too high to be useful. The proposed method has high similarity (77.9% in total).

The mean shortest distance error, standard deviation, and maximum value between these three algorithms' contours and doctors' manual contours are listed in Table 3.3. The proposed method has the smaller shortest distance error (6.9 pixels), standard deviation (3.9 pixels), and maximum value (16.1 pixels). Figure 3.11 is TP versus FP

plotting Figure, which was used in clinical data analysis [77]. The proposed method yields estimate in the upper left corner of ROC which provided high sensitivity and specificity than other two methods.

Table 3.3. Shortest Distance Comparison among Three Algorithms.

	AC	TE	Proposed method
Mean shortest distance	24.8 pixels	41.7 pixels	6.9 pixels
Standard Deviation	17 pixels	29 pixels	3.9 pixels
Maximum Value	76.9 pixels	92.7 pixels	16.1 pixels

Another problem in BUS segmentation is handling non-tumor images. A TE method does not work for non-tumor BUS images. It always returns a tumor area. I tested the proposed method with 20 non-tumor images; 15 of them got correct results.

Because the proposed algorithm does not use an iterative method to determine the boundaries, the computation time is much less than that of the other two methods. The computational times for active contour methods, texture-based methods, and the proposed method are 65 seconds, 62 seconds, and 4 seconds, respectively. The experiments used BUS images of the size 450x400, Matlab 2008, Pentium D 3.00GHZ, and 3GB RAM.

3.4 Conclusions

In this chapter, neutrosophy is employed in BUS image segmentation. It integrates the two controversial opinions about speckles: speckles are noise versus speckles include pattern information. The proposed method is fully automatic, effective, and

robust. It can segment entire BUS images without manual initialization. The method is also faster than other methods. The experiment results show that the proposed method can segment low contrast BUS images with high accuracy.

(a)

(b)

(c)
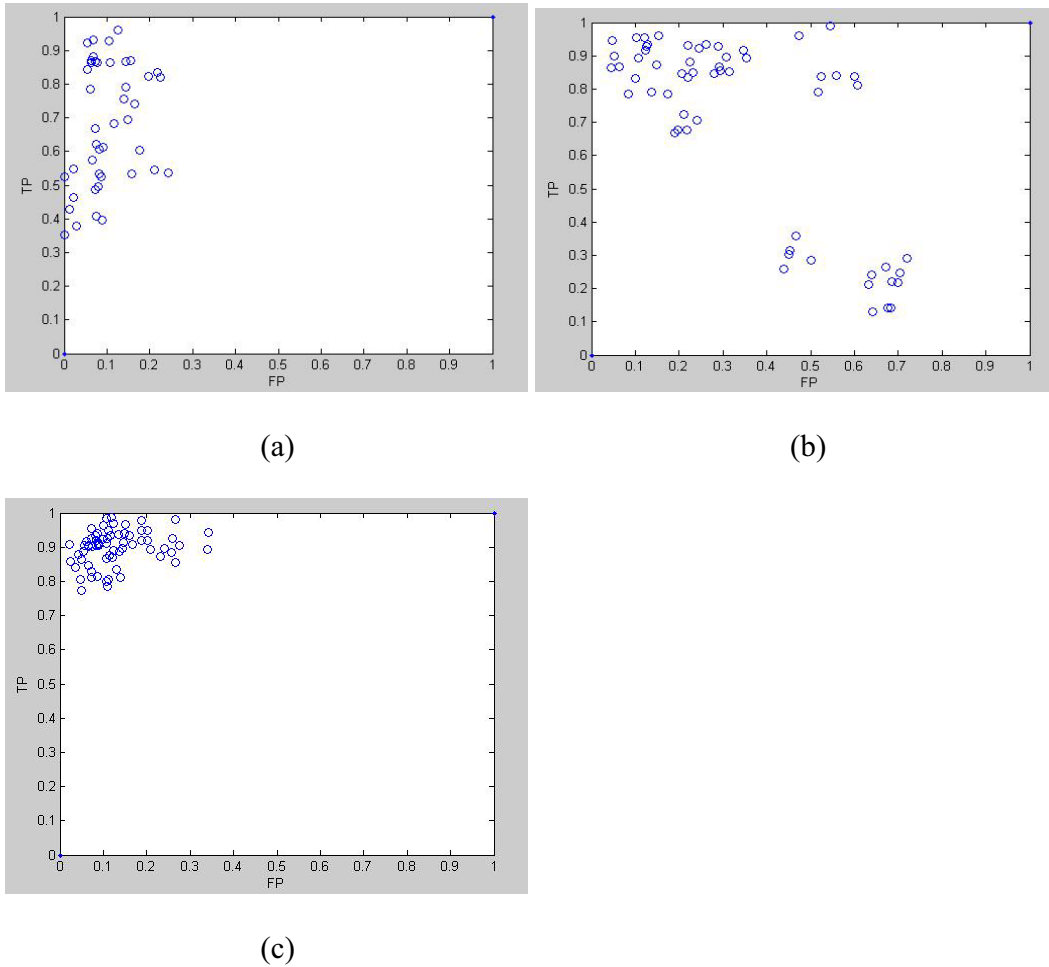
Figure 3.11. TP versus FP plotting. (a) Plotting of activate contour method. (b) Plotting of TE method. (c) Plotting of proposed method.

CHAPTER 4

COLOR IMAGE SEGMENTATION

BASED ON NEUTROSOPHY

4.1 Introduction

Color images contain more information than do gray level images, and they are more close to the real-world [97-98]. The human eye can distinguish thousands of color shades and intensities but only two-dozen shades of gray. Quite often, objects that cannot be extracted using a gray scale can be extracted using color information. Relatively inexpensive color cameras are nowadays available. In digital image libraries, large collections of images and videos are color. They need to be catalogued, ordered, and stored for efficient browsing and retrieval of visual information [99-100]. Although color information permits a more complete representation of images, processing color images requires more computation time than that needed for gray level images.

Unlike gray level images, several color spaces exist for representing a color image, such as RGB, HIS, YIQ, YUV, and CIE. Table 4.1 lists the advantages and disadvantages of these color spaces.

RGB is the most commonly used model in television systems and digital cameras. While RGB is suitable for color display, it is not good for color scene segmentation and analysis due to the high correlation among the R, G, and B [101-102]. High correlation means that if the intensity changes, all the three components will change accordingly. The measurement of a color in RGB space does not represent color differences in a

Table 4.1. Comparison of Different Color Spaces [97].

Color space	Advantages	Disadvantages
RGB	Easy to display.	High correlation.
HSI	Based on human color perception. H can be used for separating objects with different colors.	Singularity and numerically unstable at low saturation due to non-linear transformation.
YIQ and YUV	Less computation time. Partly gets rid of the correlation of RGB. Y is good for edge detection.	Correlation still exists due to the linear transformation from RGB.
CIE (L*u*v*)	Color and intensity information are independent. Efficient in measuring small color difference.	Has the same singularity problem as other non-linear transformations do.

uniform scale. It is impossible to evaluate the similarity of two colors from their distance in an RGB space.

A hue-saturation-intensity (HSI) system is another often used color space in image processing. It is more intuitive to human vision [103-104]. There exist several variants of HSI systems, such as hue-saturation-brightness (HSB), hue-saturation-lightness (HSL), and hue-saturation-value (HSV). An HSI system separates color information from intensity information. Color information is represented by hue and saturation values, while intensity, which describes the brightness of the image, is determined by the amount of light. Hue represents basic colors and is determined by the dominant wavelength in the spectral distribution of light. Saturation is a measure of the purity of

color and signifies the amount of white light mixed with the hue. Figure 4.1 is a geometrical description of HSI [105]. Hue is considered as an angle between a reference line and the color point in RGB space with the range value from 0° to 360°. For example, green is 120° and blue is 240°. The saturation component represents the radial distance from the cylinder center. The nearer the point is to the center, the lighter the color. Intensity is the height in the axis direction. For example, 0 intensity is black, full intensity is white. Each slice of the cylinder has the same intensity. Because human vision system can easily distinguish the difference of hue, HSI has a good ability to represent the human color perception. The following formulas transfer RGB to HSI:

$$H = \arctan\left(\frac{\sqrt{3}(G-B)}{(R-G)+(R-B)}\right)$$

$$Int = \frac{(R+G+B)}{3}$$

$$Sat = 1 - \frac{\min(R,G,B)}{l}$$
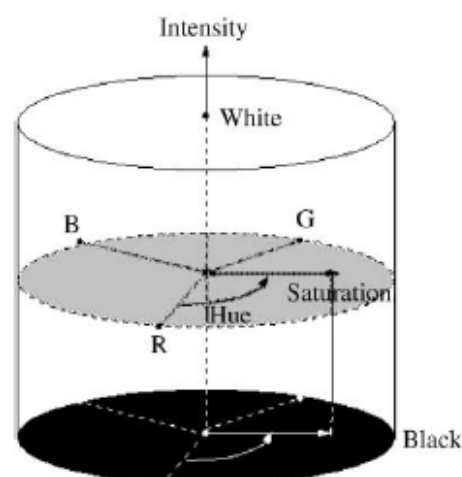
Figure 4.1 HSI color space [105].

YIQ is used to encode color information in TV signals in the American system. Y is a measure of the luminance of the color, and is a possible candidate for edge detection. I and Q are components jointly describing image hue and saturation [106]. The YIQ color space can partly get rid of the correlation of RGB color space, and the linear transformation needs less computation time than the nonlinear transformation. YIQ is obtained from the RGB by a linear transformation:

$$\begin{bmatrix} X \\ Y \\ Z \end{bmatrix} = \begin{bmatrix} 0.299 & 0.587 & 0.114 \\ 0.596 & -0.274 & -0.322 \\ 0.211 & -0.253 & -0.312 \end{bmatrix} \begin{bmatrix} R \\ G \\ B \end{bmatrix}$$

where $0 \le R \le 1, 0 \le G \le 1, 0 \le B \le 1$.

YUV is another TV color representation and is used in the European TV system. The transformation formula is:

$$\begin{bmatrix} X \\ Y \\ Z \end{bmatrix} = \begin{bmatrix} 0.299 & 0.587 & 0.114 \\ -0.147 & -0.289 & 0.437 \\ 0.615 & -0.515 & -0.100 \end{bmatrix} \begin{bmatrix} R \\ G \\ B \end{bmatrix}$$

where $0 \le R \le 1, 0 \le G \le 1, 0 \le B \le 1$.

The Commission International de l'Eclairage (CIE) color space was created to represent perceptual uniformity. It meets the psychophysical need for a human observer. Three primaries in CIE is denoted as X, Y, and Z. Any color can be specified by the combination of X, Y, and Z. The value of X, Y, and Z can be computed by a linear transformation from RGB. Here is an example of the National Television System Commission, United States (NTSC) transformation matrix:

$$\begin{bmatrix} X \\ Y \\ Z \end{bmatrix} = \begin{bmatrix} 0.607 & 0.174 & 0.200 \\ 0.299 & 0.587 & 0.114 \\ 0.000 & 0.066 & 1.116 \end{bmatrix} \begin{bmatrix} R \\ G \\ B \end{bmatrix}$$

There are a number of CIE spaces that can be created if the XYZ tristimulus coordinates are known. For example, CIE(L*a*b*) and CIE(L*u*v*) are two typical CIE spaces. The definition of CIE(L*a*b*) is:

$$L* = 116 \cdot (\sqrt[3]{\frac{Y}{Y_0}}) - 16$$

$$a* = 500\left[\sqrt[3]{\frac{X}{X_0}} - \sqrt[3]{\frac{Y}{Y_0}}\right]$$

$$b* = 500\left[\sqrt[3]{\frac{Y}{Y_0}} - \sqrt[3]{\frac{Z}{Z_0}}\right]$$

where $Y/Y_0 > 0.01$, $X/X_0 > 0.01$, and $Z/Z_0 > 0.01$. X_0, Y_0, Z_0 are X, Y, Z values for the standard white. The definition of CIE(L*u*v*) is given in the next section. The difference of two colors in these two spaces can be calculated as the Euclidean distance between two color points like this: $\Delta E_{ab} = \sqrt{(\Delta L*)^2 + (\Delta a*)^2 + (\Delta b*)^2}$ or $\Delta E_{ab} = \sqrt{(\Delta L*)^2 + (\Delta u*)^2 + (\Delta v*)^2}$. Euclidean distance has the ability to express the color difference of human perception. (L*a*b*) and (L*u*v*) are approximately a uniform chromaticity scale, which matches the sensitivity of human eyes in computer processing [107], whereas RGB and XYZ color space do not have such properties. HSI can be mapped to the cylindrical coordinates of (L*a*b*) or (L*u*v*) space by these:

HSI to CIE(L*a*b*)

$I = L*$

$H = \arctan(a*/b*)$

$S = \sqrt{(a*)^2 + (b*)^2}$

and

HSI to CIE(L*u*v*)

$I = L*$

$H = \arctan(u*/v*)$

$S = \sqrt{(u*)^2 + (v*)^2}$

(L*a*b*) and (L*u*v*) share the same L* value, which defines the lightness, or the intensity of a color. CIE spaces can control color and intensity information more independently and simply than RGB space. Direct color comparison can be performed based on geometric separation within the color space. Therefore, CIE space is especially efficient in measuring small color differences.

Most color image segmentation methods are based on gray level image segmentation approaches with different color representations. The authors of [97, 108] mention that color images can be considered as a special case of multi-spectral images, and any segmentation method for multi-spectral images can be applied to color images, see Figure 4.2 [97]. Most gray level segmentation techniques can be extended to color images, such as histogram thresholding, clustering, region growing, edge detection, etc. Gray level segmentation methods can be directly applied to each component of a color space. The results next are combined in some way to get the final segmentation result [109]. But there exist two problems:

| Color Segmentation Methods | —— —— | Gray level segmentation Methods

Histogram-based
Space Clustering
Edge-based
Region-based
Neural Network
Fuzzy Logic | + | Color Spaces
RGB
HSI
YIQ
YUV
CIE(L*a*b*)
CIE(L*u*v*) |
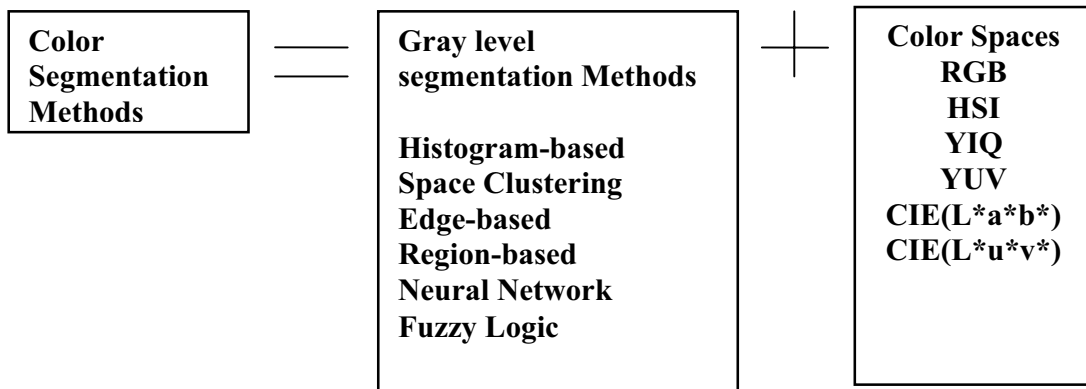
Figure 4.2 Relationship between gray level segmentation and color segmentation.

1. When the color is projected onto three components, the color information is scattered such that the color image becomes simply a multispectral image and the color information that humans can perceive is lost.

2. Each color representation has its advantages and disadvantages. There is no single color representation than surpasses others for segmenting all kinds of color images.

Most of existing color image segmentation methods define a region based on similarity of color. This assumption often makes it difficult for algorithms to separate the objects with highlights, shadows, shadings, or texture. This causes inhomogeneity of colors. Most color segmentation methods are only conducted in one color space [97, 110-111]. Color segmentation techniques can be grouped into several categories: histogram methods, space clustering methods, edge-based methods, region-based methods, neural network

methods, and fuzzy logic methods [97]. Table 4.2 gives a comparison of the segmentation techniques [97].

Table 4.2. Comparison of Different Segmentation Techniques [97].

Technique	Advantages	Disadvantages
Histogram	Unsupervised method. Low time complexity.	Does not work well for image without obvious peaks or valleys. Does not include spatial information.
Edge-based method	Low time complexity.	Over-segmentation. Noise sensitive.
Region-based method	Noise tolerant than edge-based method.	High time complexity. Seed selection is important. Boundary points may be clustered into wrong region.
Neural network approaches	Utilize existing neural network. Low time complexity for execution.	Training time is long, training data are important. Overtraining problem.
Fuzzy logic approaches	Fuzzy membership can be used to represent the degree of some properties. Use both global and local information.	Determination of fuzzy membership is not a trivial job. Time complexity is high.

A histogram algorithm is one of the most widely used techniques for gray image segmentation [112]. It assumes that images are composed of regions with different gray level ranges. The histogram of an image can be separated into peaks, each corresponding

to one region. There is a threshold value for separating two adjacent peaks. In color images, the situation is different from a gray image because of multi-features. Multiple histogram-based thresholding divides a color space by thresholding each component histogram. There is a limitation when dividing multiple dimensions, however, because thresholding is a technique for gray scale images. In many approaches, thresholding is performed on only one color component at a time. Thus, the regions extracted are not based on the information available from all three components simultaneously. The correlation among the three components is neglected.

Edge-based techniques are extensively utilized in gray level image segmentation. They are based on the detection of discontinuity and locating points with abrupt changes in gray level. Edge-based methods are usually classified into two categories: sequential and parallel [113]. In color images, the information about edges is much richer than that in gray images. For example, edges between two objects with the same brightness but different hue can be detected in color images [114]. Accordingly, in a color image, an edge should be defined by a discontinuity in a three-dimensional color space. There are three alternatives for the definition of a color edge:

1. Define a metric distance in some color space, and use discontinuities in the distance to determine edges [115].

2. Regard a color image as composed of three gray images formed by the three color components, respectively. Perform gray level edge detection on these three images separately. Then, the edges detected in the three images are merged by specified procedures [116-117].

3. Impose some uniformity constraints on the edges in the three color components to utilize all of the three color components simultaneously, but allow the edges in the three color components to be largely independent [115].

Region-based techniques include region growing, region splitting, region merging, and their combination. In the region growing approach, seed regions are first selected, then expanded to include all homogeneous neighbors. This process is repeated until all pixels in the image are classified. One problem with region growing is its dependence on the selection of a seed region and the order in which pixels and regions are examined. In region splitting techniques, the initial seed region is simply the whole image. If the seed region is not homogeneous, it is usually divided into four, squared subregions, which become new seed regions. The process repeats until all sub-regions are homogeneous. The disadvantage of region splitting is that the resulting regions come out too square. These methods work best on images with an obvious homogeneity criterion. However, all region-based approaches are by nature sequential, and dependence on the selection of seed regions and the order in which pixels and regions are examined [118-120].

Artificial neural networks (ANN) are widely applied for pattern recognition. Neural networks are composed of many computational elements connected by links with variable weights. There are different neural networks used in image segmentation such as backprogagation (BP) [121-122], Hopfield neural networks (HNN) [123-124], and self-organizing maps (SOM) [125-127]. One problem with neural network techniques is that training time is very long. The selection of training and testing sets is also important.

Fuzzy logic techniques provide a mechanism to represent and manipulate uncertainty and ambiguity. Fuzzy operators, properties, mathematics, and inference rules have found considerable application in image segmentation [128-130]. In fuzzy subsets, each pixel in an image has a degree to which it belongs to a region or a background, characterized by a membership value. In color images, the colors tend to form clusters in the color space which can be regarded as a natural feature space. One problem with traditional clustering techniques is that there are only two values, 1 or 0, to indicate to what degree a data point belongs to a cluster. This problem can be solved by using fuzzy set methods. But fuzzy logic also has its own problems, such as determining the number of clusters and high computational cost for large data sets.

In this chapter, I define <A> in an RGB color space and define <Neut-A> in a CIE (L*u*v*) color space. By introducing <Neut-A>, the proposed algorithm can combine both color and spatial information. It also uses the information of two color spaces, and utilizes both global and local information of color image. Figure 4.3 is the flowchart of the proposed algorithm.
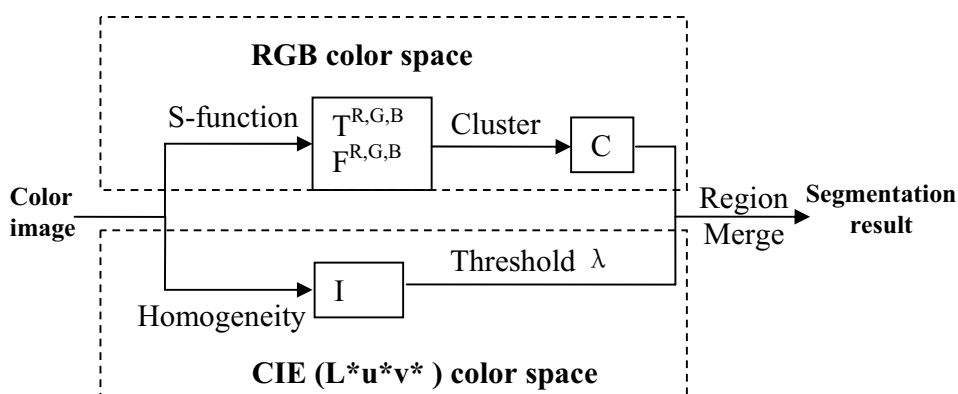
Figure 4.3. Flowchart of proposed method.

4.2 Proposed Method

4.2.1 Map Image in RGB Space

Given color image A, $P(x,y)$ is a pixel in A, and (x,y) is its position. A 5x5 mean filter (the size of filter may vary depending on the size of the input image) is applied on A to remove noise. A pixel of a color image in the neutrosophic domain can be represented as $A\{(T^R,T^G,T^B),I,(F^R,F^G,F^B)\}$. T^R,T^G,T^B, F^R,F^G and F^B describe the brightness in the R, G, and B subspaces, respectively. I is the indeterminacy in CIE (L*u*v*) space. The standard S-function is used. For a pixel in the R color space, the definitions of T^R and F^R are [40]:

$$T^R(x,y) = S^R(g_{xy}^R,a^R,b^R,c^R) = \begin{cases} 0 & 0 \le g_{xy}^R \le a^R \\ \dfrac{(g_{xy}^R - a^R)^2}{(b^R - a^R)(c^R - a^R)} & a^R \le g_{xy}^R \le b^R \\ 1 - \dfrac{(g_{xy}^R - c^R)^2}{(c^R - b^R)(c^R - a^R)} & b^R \le g_{xy}^R \le c^R \\ 1 & g_{xy}^R \ge c^R \end{cases} \qquad (2.1)$$

$$F^R(x,y) = 1 - T^R(x,y) \qquad (2.2)$$

where g_{xy}^R is the intensity value of pixel $P(x,y)$ in R. Variables a^R, b^R, and c^R are the parameters that determine the shape of the S-function in subspace R.

We will use the maximum entropy principle method to calculate the parameters a^R, b^R, and c^R. The corresponding entropy is defined as

$$H^R(X) = \frac{1}{M \times N} \sum_{i=1}^{M} \sum_{j=1}^{N} S_n^R \left(T^R(x,y) \right) \qquad (2.3)$$

where $S_n^R()$ is a Shannon function which is defined as:

$$S_n^R\left(T^R(x,y)\right) = -T^R(x,y)\log_2 T^R(x,y) - \left(1-T^R(x,y)\right)\log_2\left(1-T^R(x,y)\right)$$
$$x = 1,2,\cdots,M, \text{ and } y = 1,2,\cdots,N \tag{2.4}$$

Again, the maximum entropy principle states: the greater the entropy is, the more information the system has [16, 43-44]. To find the optimal b^R, try every $b^R \in [a^R+1, c^R-1]$. The optimal b^R will result in the maximum entropy, $H^R(X)$:

$$H_{max}^R(X,a^R,b_{opt}^R,c^R) = \max\{H^R[X;a^R,b^R,c^R] \mid g_{min}^R \le a^R < b^R < c^R \le g_{max}^R\} \tag{2.5}$$

a^R and c^R are calculated by following steps:

(1) Calculate the histogram of the image

(2) Find the local maxima of the histogram: $His_{max}(g_1^R), His_{max}(g_2^R), ... His_{max}(g_n^R)$. Calculate the mean of the local maxima:

$$\overline{His_{max}\left(g^R\right)} = \frac{\sum\limits_{i=1}^{n} His_{max}\left(g_i^R\right)}{n} \tag{2.6}$$

(3) Find the peaks greater than $\overline{His_{max}\left(g^R\right)}$, let the first peak be g_{min}^R and the last peak be g_{max}^R

(4) Define low limit B_1 and high limit B_2:

$$\sum_{i=g_{min}^R}^{B_1} His(i) = \varepsilon_1$$
$$\sum_{i=B_2}^{g_{max}^R} His(i) = \varepsilon_1 \tag{2.7}$$

where the information loss is allowed in the range $[g_{min}^R, B_1^R]$ and $[B_2^R\ g_{max}^R]$, which is ε_1 (we choose $\varepsilon_1 = 0.01$ based on experimental results).

(5) Determine a^R and c^R

$$a^R = (1-f)(g_1^R - g_{min}^R) + g_{min}^R$$
$$if\,(a^R > B_1^R) \qquad then \qquad a^R = B_1^R$$

(2.8)

$$c^R = f(g_{max}^R - g_n^R) + g_n^R$$
$$if\,(c^R > B_2^R) \qquad then \qquad c^R = B_2^R$$

(2.9)

where $f = 0.01$, and B_1^R and B_2^R are used to avoid important information loss. The pixel whose intensity is less than B_1^R is considered as background, and the pixel whose intensity is greater than B_2^R is considered as noise.

After a^R, b^R, and c^R are determined, we get T^R and F^R according to Eq. 4.1. Similarly, we can determine T^G, T^B, F^G, and F^B in corresponding subspaces.

4.2.2 Enhancement

Use an intensification transformation to do enhancement, and calculate newly enhanced T_E^k in the corresponding R_E, G_E and B_E color subspaces [10]:

$$T_E^k = E(T^k(x,y)) = 2(T^k(x,y))^2 \qquad\qquad 0 \leq T^k(x,y) \leq 0.5$$
$$T_E^k = E(T^k(x,y)) = 1 - 2(1-T^k(x,y))^2 \qquad\qquad 0.5 < T^k(x,y) \leq 1$$

(2.10)

where $k \in \{R, G, B\}$. Figure 4.4(a) is a 512x512 color Lena image. Figure 4.4(b) is the result after applying the S-function and enhancement.

4.2.3 Initial Cluster Centers Selection
Based on Color Information

In color segmentation, the initialization of cluster centers (seeds) is very important. Many color segmentation methods are based on iterative calculation or even manual

initialization [131]. In this paper, we use a histogram-based method to do it automatically.

(1) In enhanced color subspace R_E, equally divide the subspace into 20 bins. Calculate the histogram based on these bins.

(2) Find the local maxima: $His_{\max}(g_1^{R_E}), His_{\max}(g_2^{R_E}), ...His_{\max}(g_l^{R_E})$.

(3) Use intensity values to represent the local maxima $C^{R_E} = \{g_1^{R_E}, g_2^{R_E}, ..., g_l^{R_E}\}$.

(4) Similarly, find the local maxima in enhanced subspaces G_E and B_E.

$C^{G_E} = \{g_1^{G_E}, g_2^{G_E}, ..., g_m^{G_E}\}$ and $C^{B_E} = \{g_1^{B_E}, g_2^{B_e}, ..., g_q^{B_E}\}$.

(5) Use all of the combinations of the cal maxima in 3 subspaces as the initial cluster centers: $C = \{(g_u^{R_E}, g_v^{G_E}, g_w^{B_E})\}$, $1 \le u \le l$, $1 \le v \le m$, $1 \le w \le q$.

4.2.4 Decide Clusters on T_E^k

After the initial cluster centers are decided, assign pixels to clusters based on the distance to each center.

(1) For a pixel $P(t^{R_E}, t^{G_E}, t^{B_E})$, calculate the distances to all cluster centers by Euclidean distance. Here, $t^{R_E} \in T_E^R$, $t^{G_E} \in T_E^G$, and $t^{B_E} \in T_E^B$.

$$Dist_i(P) = \sqrt{(t^{R_E} - g_u^{R_E})^2 + (t^{G_E} - g_v^{G_E})^2 + (t^{B_E} - g_w^{B_E})^2} \qquad (2.11)$$

where $Dist_i(P)$ is the distance between pixel P and cluster center $C_i(g_u^{R_E}, g_v^{G_E}, g_w^{B_E})$. Here, C_i is the ith center in C.

(2) Assign pixel P to the cluster with the minimum distance.

(3) If the size of any cluster is less than 5x5, delete the corresponding center from the

cluster center set.

(4) Update each cluster center by the value of pixels assigned to it.

$$C_i' = \{\frac{\sum_{j=1}^{m} t_j^{R_E}}{m}, \frac{\sum_{j=1}^{m} t_j^{G_E}}{m}, \frac{\sum_{j=1}^{m} t_j^{B_E}}{m}\} \tag{2.12}$$

where C_i' is the new center to replace C_i; m is the number of pixels assigned to

C_i; and $t_j^{R_E}, t_j^{G_E}$ and $t_j^{B_E}$ are the values of pixel P_j assigned to C_i.

(5) Repeat steps (1)-(4) until the distance of the maximum center change is less than

0.1.

(6) Segment image into regions $R_1, R_2....R_n$ by using cluster centers calculated in the

above steps. See Figure 4.4(c).

4.2.5 Define Indeterminacy I in CIE(L*u*v*)

CIE (L*u*v*) color space does well at measuring small color differences, while

RGB does not [132]. The conversion of RGB to CIE (L*u*v*) is [133]:

$$\begin{bmatrix} X \\ Y \\ Z \end{bmatrix} = \begin{bmatrix} 0.490 & 0.310 & 0.200 \\ 0.177 & 0.813 & 0.011 \\ 0.000 & 0.010 & 0.990 \end{bmatrix} \begin{bmatrix} R \\ G \\ B \end{bmatrix}$$

$$u' = \frac{4X}{X+15Y+3Z} = \frac{4x}{-2x+12y+3} \tag{2.13}$$

$$v' = \frac{9Y}{X+15Y+3Z} = \frac{9y}{-2x+12y+3}$$

$$L^* = \begin{cases} 116 \cdot (\frac{Y}{Y_n})^{\frac{1}{3}} - 16, & \frac{Y}{Y_n} > (\frac{6}{29})^{\frac{1}{3}} \\ (\frac{29}{3})^3 \cdot \frac{Y}{Y_n} & \frac{Y}{Y_n} \le (\frac{6}{29})^{\frac{1}{3}} \end{cases}$$

$$u^* = 13L^* \cdot (u' - u'_n) \qquad\qquad (2.14)$$

$$v^* = 13L^* \cdot (v' - v'_n)$$

We define indeterminacy I by using the standard deviation and discontinuity in the CIE space. Standard deviation describes the contrast within a local region, while discontinuity represents the edge. Both of them contain spatial information.

A size $d \times d$ window centered at (x, y) is used for computing the standard deviation of pixel $P_{(x,y)}(L, u, v)$ in subspaces L^*, u^* and v^*, respectively:

$$sd^{L^*}(x, y) = \sqrt{\frac{\sum_{p=x-(d-1)/2}^{x+(d-1)/2} \sum_{q=y-(d-1)/2}^{y+(d-1)/2} (L_{pq} - \mu^{L^*}_{xy})^2}{d^2}}$$

$$sd^{u^*}(x, y) = \sqrt{\frac{\sum_{p=x-(d-1)/2}^{x+(d-1)/2} \sum_{q=y-(d-1)/2}^{y+(d-1)/2} (u_{pq} - \mu^{u^*}_{xy})^2}{d^2}} \qquad (2.15)$$

$$sd^{v^*}(x, y) = \sqrt{\frac{\sum_{p=x-(d-1)/2}^{x+(d-1)/2} \sum_{q=y-(d-1)/2}^{y+(d-1)/2} (v_{pq} - \mu^{v^*}_{xy})^2}{d^2}}$$

where $\mu^{L^*}_{xy}, \mu^{u^*}_{xy}$ and $\mu^{v^*}_{xy}$ are the means of the color values within the window in L^*, u^* and v^*, respectively.

$$\mu^{L^*}{}_{xy} = \frac{\displaystyle\sum_{p=x-(d-1)/2}^{x+(d-1)/2}\sum_{q=y-(d-1)/2}^{y+(d-1)/2} L_{pq}}{d^2}$$

$$\mu^{u^*}{}_{xy} = \frac{\displaystyle\sum_{p=x-(d-1)/2}^{x+(d-1)/2}\sum_{q=y-(d-1)/2}^{y+(d-1)/2} u_{pq}}{d^2}$$

$$\mu^{v^*}{}_{xy} = \frac{\displaystyle\sum_{p=x-(d-1)/2}^{x+(d-1)/2}\sum_{q=y-(d-1)/2}^{y+(d-1)/2} v_{pq}}{d^2}$$

The discontinuity of pixel $P_{(x,y)}(L,u,v)$ is described by the edge value, which is calculated by the Sobel operator in subspaces L^*, u^* and v^*, respectively:

$$eg^{L^*}(x,y) = \sqrt{(G_x^{L^*})^2 + (G_y^{L^*})^2}$$
$$eg^{u^*}(x,y) = \sqrt{(G_x^{u^*})^2 + (G_y^{u^*})^2} \qquad (2.16)$$
$$eg^{v^*}(x,y) = \sqrt{(G_x^{v^*})^2 + (G_y^{v^*})^2}$$

where $G_x^{L^*}, G_x^{u^*}, G_x^{v^*}$ and $G_y^{L^*}, G_y^{u^*}, G_y^{v^*}$ are the horizontal and vertical derivative approximations in L^*, u^* and v^*, respectively.

Normalize the standard deviation and discontinuity:

$$sd_{Norm}(x,y) = \frac{sd(x,y)}{sd_{max}} \qquad (2.17)$$

$$eg_{Norm}(x,y) = \frac{eg(x,y)}{eg_{max}} \qquad (2.18)$$

Define the indeterminacy as:

$$I(x,y) = \sqrt{(sd_{Norm}^{L^*}(x,y) \cdot eg_{Norm}^{L^*}(x,y))^2 + (sd_{Norm}^{u^*}(x,y) \cdot eg_{Norm}^{u^*}(x,y))^2 + (sd_{Norm}^{v^*}(x,y) \cdot eg_{Norm}^{v^*}(x,y))^2}$$
$$(2.19)$$

Normalize I

$$I_{Norm}(x, y) = \frac{I(x, y)}{I_{max}} \qquad (2.20)$$

Figure 4.4(e) is the indeterminacy image in domain I. The value of $I_{Norm}(x, y)$ has a range of [0, 1]. The more uniform the region surrounding a pixel is, the smaller the indeterminacy value of the pixel. The window size should be big enough to include enough local information, but still smaller than the distance between two objects. We chose d = 7 in our experiments.

4.2.6 Region Merging Based on T_E, F_E, and I_{Norm}

The clusters segmented in T_E are based on color information in an RGB space. The edges in I_{Norm} include the spatial information in a CIE space. We get the final segmentation result based on the following:

$$R_i \bigcup_{i \neq j} R_j = \begin{cases} true & if\ R_i \cap R_j \neq \phi\ and\ avg(I_{norm}(R_i \cap R_j)) \geq \lambda \\ false & otherwise \end{cases} \qquad (2.21)$$

where R_i and R_j are regions calculated in subsection 2.4. $R_i \cap R_j$ are intersection pixels of regions R_i and R_j. $avg(I_{norm}(R_i \cap R_j))$ is the average indeterminate value of the intersection pixels.

Figure 4.4(f) is the final segmentation result of Lena based on I_{Norm} with $\lambda = 0.04$. Figure 4.4(g) is the boundaries of (f). Adding indeterminacy reduces over-segmentation.

(a)　　　　　　　　　(b)　　　　　　　　　(c)

(d)　　　　　　　　　(e)　　　　　　　　　(f)

(g)
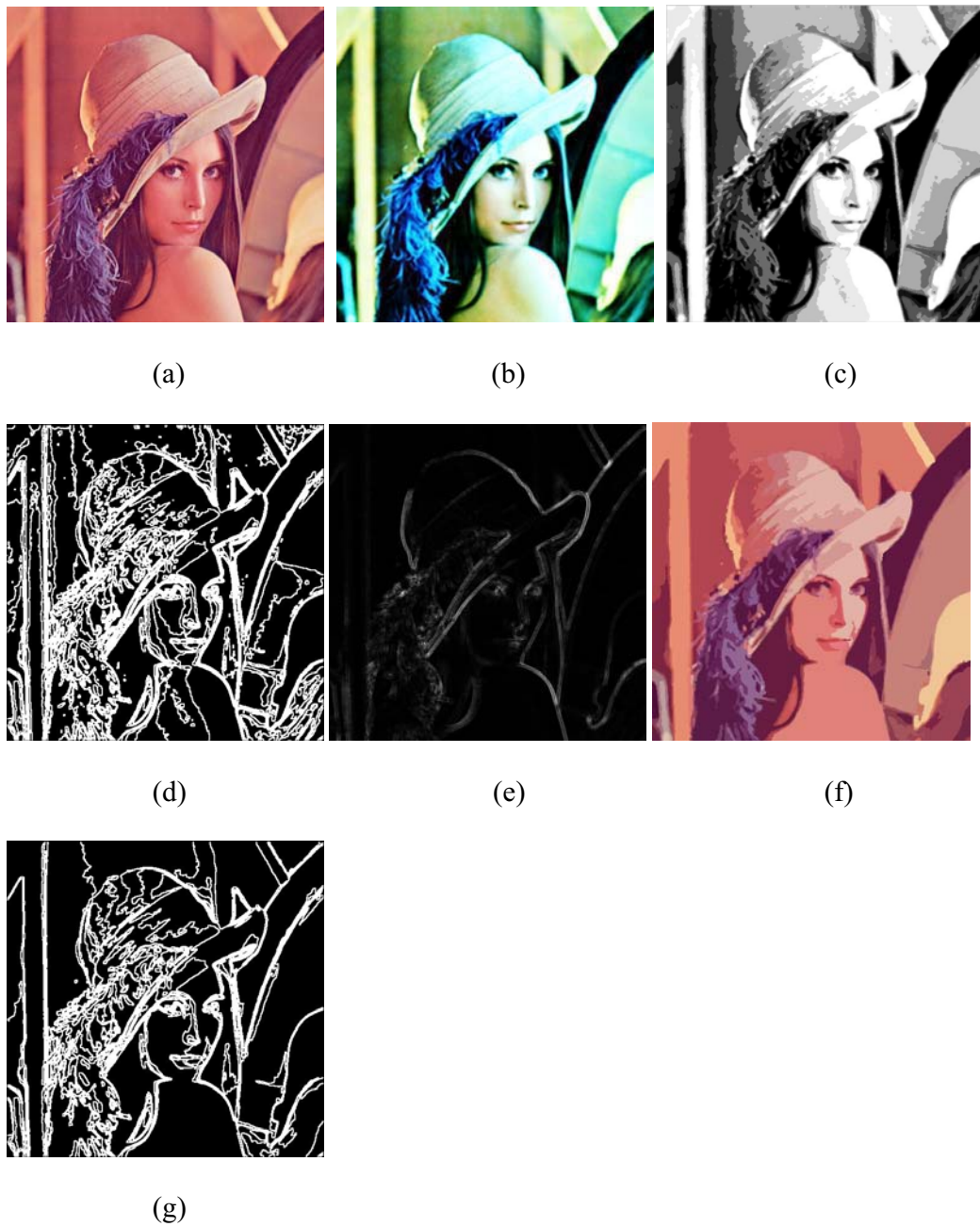
Figure 4.4. Steps of proposed algorithm: (a) 512x512 Lena color image. (b) Result after applying the S-function and enhancement. (c) Clusters result in T. (d) Boundaries based on (c). (e) Indeterminacy value image in I. (f) Final result of the proposed segmentation method ($\lambda = 0.04$). (g) Boundaries of (f).

4.3 Experimental Results

Domains T and F use the histograms, which include the global information. Domain I includes the local information. By combining T, F and I, the proposed algorithm can utilize both global and local information very well.

4.3.1 Parameter λ

Parameter λ is very important to performance. It controls the segmentation result. The higher the λ value is, the fewer clusters there are in the segmentation result. Figures 4.5(a), (b), and (c) show the results of $\lambda = 0.01$, 0.05, and 0.1. Figures 4.5(d), (e), and (f) are the corresponding boundary images of (a), (b) and (c). The numbers of clusters are 524, 393, and 290, respectively.

4.3.2 Comparison with Other Fuzzy Logic Algorithms

Neutrosophy is an extension to fuzzy logic. We now compare our approach with several fuzzy logic color segmentation methods to show the advantage of neutrosophy.

Figure 4.6(a) is a 283x283 meadow image, and Figure 4.7(a) is a 256x256 house image. Figure 4.6(b) and Figure 4.7(b) are the segmentation results after applying the traditional fuzzy c-mean (FCM) algorithm, which is a widely used, unsupervised segmentation method [13, 134-135]. Figure 4.6(c) and Figure 4.7(c) are the boundary results of Figure 4.6(b) and Figure 4.7(b), respectively. There are 3757 regions in Figure 4.6(b) and 1673 regions in Figure 4.7(b). We can see that the traditional FCM produces over-segmentation, and the boundaries are not clear. Figure 4.6(e) and Figure 4.7(e) are the results of a modified FCM method (FCM_M) [23], which uses an adaptive method

to initialize cluster centers. It reduces over-segmentation (2913 regions in Fig. 5(e) and 1007 regions in Figure 4.7(e)) much better than does a traditional FCM. However, it still includes over-segmentation on the right lower roof and eaves. Figure 4.6(f) and Figure 4.7(f) are the results of the proposed method (Neut). The over-segmentations are greatly reduced (47 regions in Figure 4.6(f) and 69 regions in Figure 4.7(f)). Sheep boundaries in Figure 4.6(f) and details of house edges in Figure 4.7(f) are kept very well. The proposed method can outline main objects very well and has fewer regions than fuzzy c-mean and modified fuzzy c-mean.

Figure 4.8(b) and Figure 4.9(b) are the segmentation results after using the fuzzy homogeneity algorithm (FHM) in [136]. It utilizes a fuzzy homogeneity histogram and scale-space filter to merge regions. Figure 4.8(d) and Figure 4.9(d) are the results after using the proposed algorithm. In Figure 4.8(b), the shape of the airplane and mountains are kept very well. The sailboat and ocean are clearly outlined in Figure 4.9(d). We can see that the fuzzy homogeneity algorithm produces more over-segmented regions than does our method (24410 regions in Figure 4.8(b) versus 251 regions in Figure 4.8(d); and 18968 regions in Figure 4. 9(b) versus 101 regions in Figure 4. 9(d)). Figure 4.8(c) and Figure 4.8(e) are the corresponding boundary images of 8(b) and 8(d), respectively. The proposed method generates thinner, smoother, and clearer boundaries than does the fuzzy homogeneity algorithm.

Table 4.3 lists the computation time of the proposed method on the different images. The cluster selection is the most time-consuming step, which takes two-thirds of

the total time. All experiments were conducted by using Matlab 2008, Pentium D

3.00GHZ, and 3GB RAM.

Table 4.3. Running Time.

Image Name	Lena (512x512)	Meadow (283x283)	House (256x256)	Plane (469x512)	Sailboat (325x475)
CPU time (s)	24.2	7.3	6.1	20.1	13.5

4.4 Conclusions

In this chapter, a new neutrosophic method for color image segmentation is proposed. It utilizes both RGB and CIE color spaces. By adding an indeterminacy domain, the proposed algorithm can combine both global and local information as well as information from two color spaces. Experimental results demonstrate that the proposed method is very noise-tolerant, effective, and accurate, and it can generate thin and clear boundaries in color segmentation results.

(a) (b) (c)

(d) (e) (f)
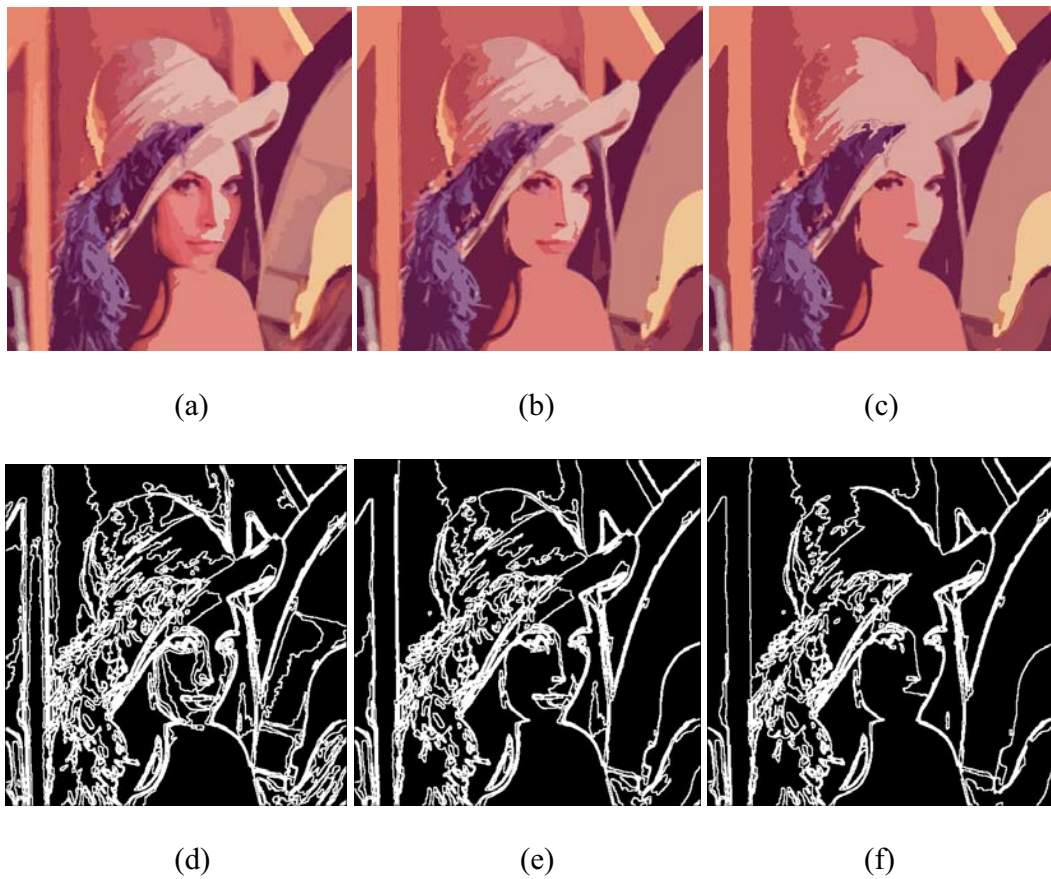
Figure 4.5. Segmentation results of different λ : (a) Segmentation result of $\lambda = 0.01$. (b) Segmentation result of $\lambda = 0.05$. (c) Segmentation result of $\lambda = 0.1$. (d) Boundaries of (a). (e) Boundaries of (b). (f) Boundaries of (c).
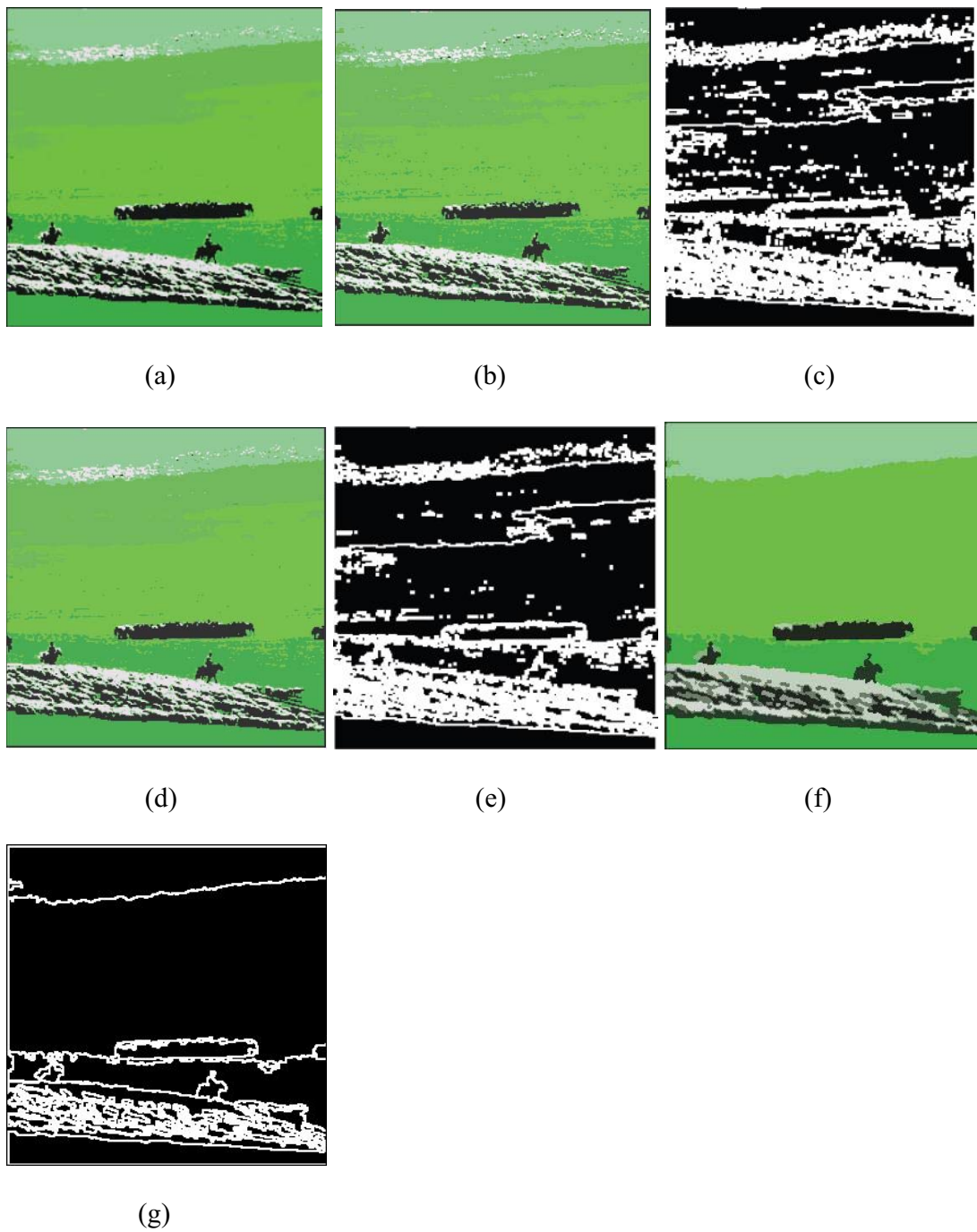
Figure 4.6. Meadow image (283x283): (a) Original image. (b) Result by applying fuzzy c-mean. (c) Boundaries of (b). (d) Result of modified fuzzy c-mean. (e) Boundaries of (e). (f) Segmentation result of the proposed method ($\lambda = 0.03$). (g) Boundaries of (f).

(a)　　　　　　　　(b)　　　　　　　　(c)

(d)　　　　　　　　(e)　　　　　　　　(f)

(g)
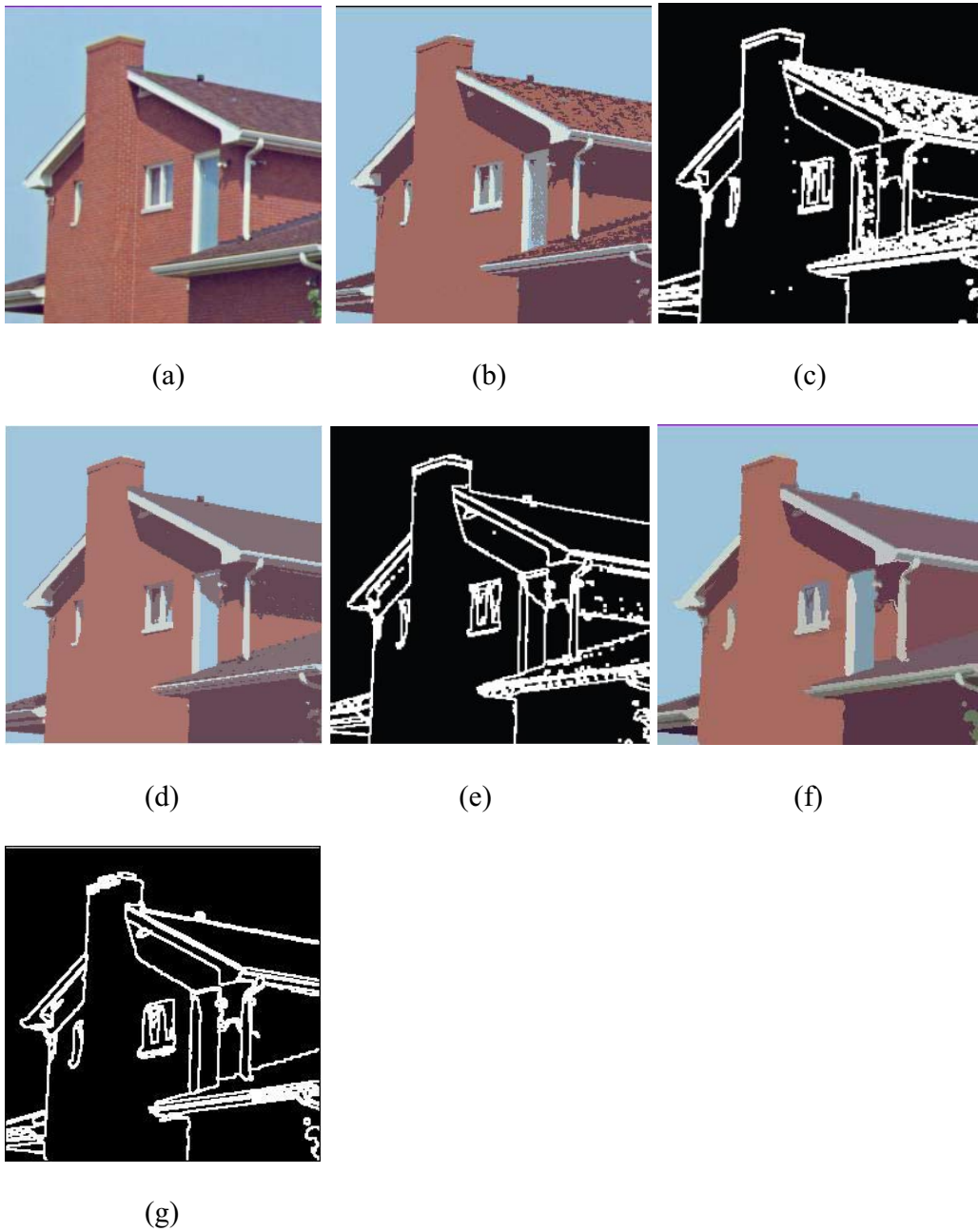
Figure 4.7. House image (256x256): (a) Original image. (c) Result by applying fuzzy c-mean. (c) Boundaries of (b). (d) Result of modified fuzzy c-mean. (e) Boundaries of (d). (f) Segmentation result of the proposed method ($\lambda = 0.03$). (g) Boundaries of (f).
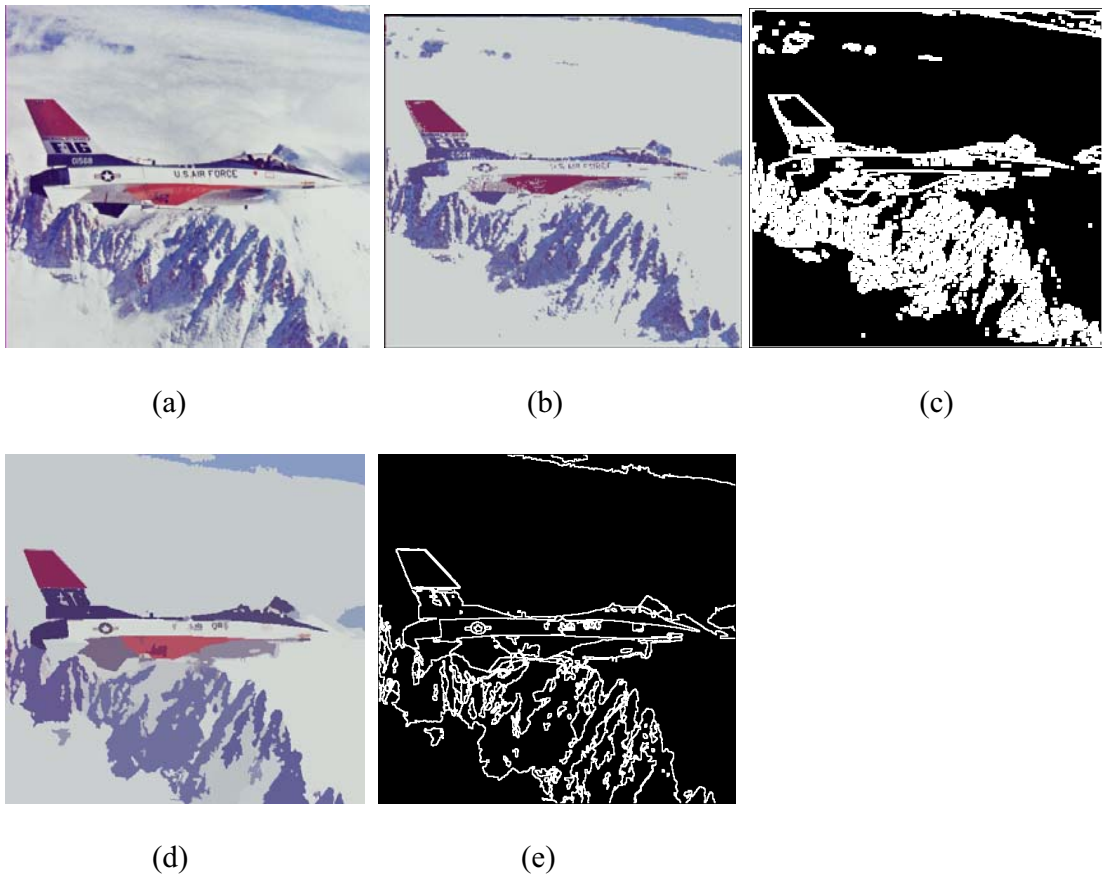
Figure 4.8. Plane image (469x512): (a) Original image. (b) Result by applying fuzzy homogeneity. (c) Boundaries of (b). (d) Segmentation result of the proposed method ($\lambda = 0.04$). (e) Boundaries of (d).

(a) (b) (c)

(d) (e)
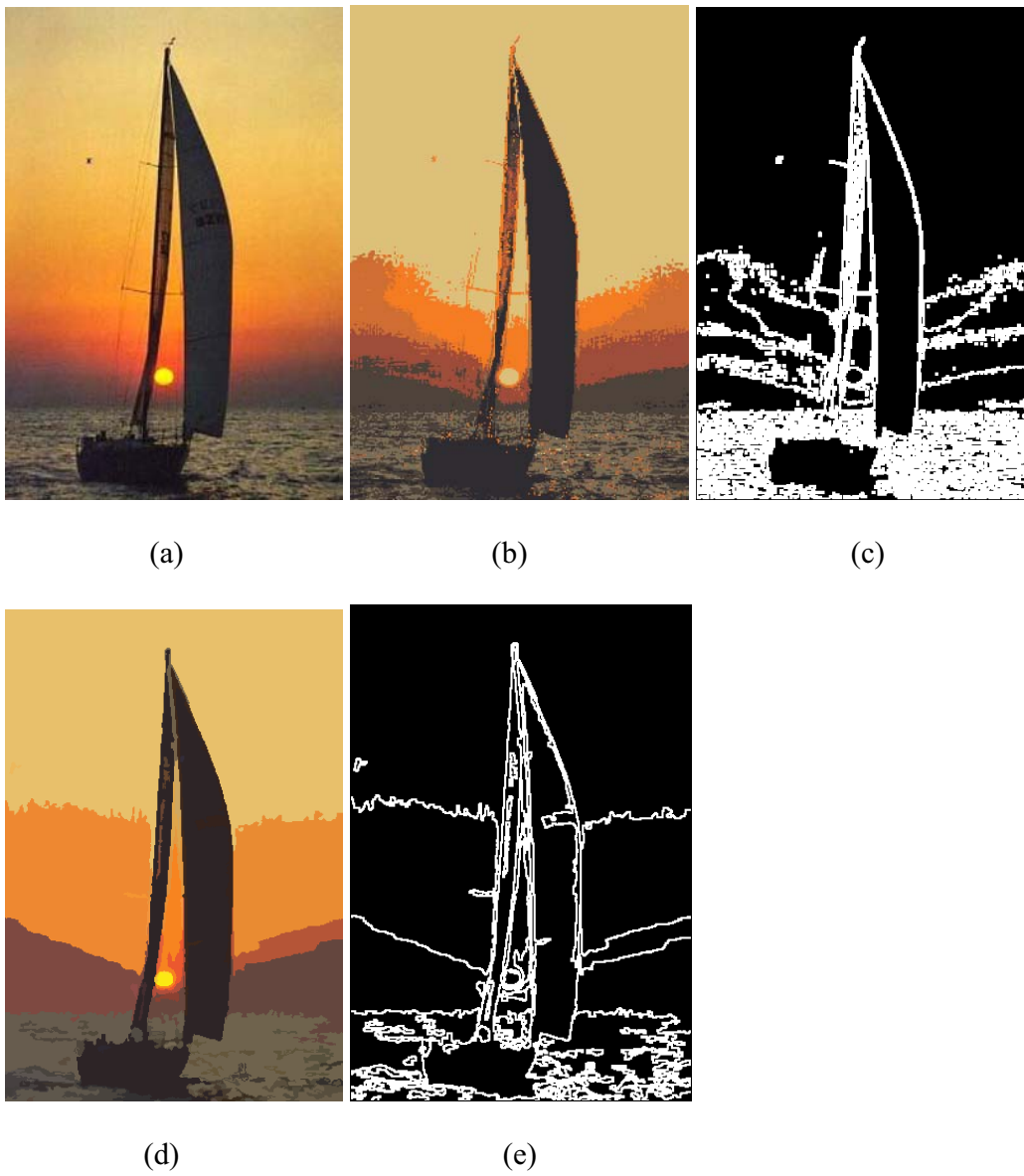
Figure 4.9. Sailboat image (325x475): (a) Original image. (b) Result by applying fuzzy homogeneity. (d) Boundaries of (b). (d) Segmentation result of the proposed method ($\lambda = 0.01$). (e) Boundaries of (d).

CHAPTER 5

CONCLUSIONS

Neutrosophy studies the origin, nature, scope of neutralities, and their interactions with different ideational spectra. It is an alternative to the existing logics and represents mathematical uncertainty, vagueness, contradiction, and imprecision.

Neutrosophy is a new philosophy that is generating discussion among philosophers and mathematicians. There is a need to find ways to implement neutrosophy in solving problems. Researchers need exposure to how T, I, F are defined and used in solving real problems.

In this dissertation, I introduce neutrosophy to image segmentation and define T, I, F in image processing. T is the degree to be the object, I is the degree to be the boundary, and F is the degree to be the background. Using neutrosophy in image segmentation increases noise-tolerant ability, and it produces a superior blurry boundary image as opposed to other methods. I apply the algorithm to breast ultrasound segmentation, which is a real problem in medical image processing. Neutrosophy helps to combine two controversial opinions about speckles: speckles are noise versus speckles include pattern information. It is also a fully automatic segmentation algorithm based on a whole BUS image not on a manually selected ROI. The experiment results give us statistical improvements over other conventional image diagnostic methods. To show neutrosophy in extended fuzzy logic, I use it in color image segmentation and compare it with different fuzzy logic algorithms. The experiments demonstrate that neutrosophy can reduce over-segmentation.

Neutrosophy is a new theory. It is an extension of fuzzy logic and can handle uncertainty and indeterminacy better than other methods. Neutrosophy may find more application in diverse fields, such as control theory, image processing, computer vision, and artificial intelligence, where fuzzy logic is applied. The future works are described as follows:

1. Neutrosophy is a new theory; the definition of indeterminacy can be defined in a different way to include more uncertainty.

2. Neutrosophy can be applied to other image processing problems like feature extraction and classification.

3. Apply neutrosophy to different research area like control theory, artificial intelligence.

REFERENCES

1   Smarandache, F. *A Unifying Field in Logics Neutrosophic Logic. Neutrosophy, Neutrosophic Set, Neutrosophic Probability*. American Research Press, 2003.

2   Zhang, M., Zhang, L., and Cheng, H.D. A neutrosophic approach to image segmentation based on watershed method. *Signal Processing 5*, 90 (2010), 1510-1517.

3   L. A. Zadeh, Fuzzy sets. *Information and Control 8*, 3 (1965), 383-353.

4   Smarandache, F. *Neutrosophy/Neutrosophic Probability, Set, and Logic*. American Research, 1998.

5   S. Florentin, Collected Papers. *Abaddaba, Oradea*, III (2000).

6   Atanassov, K. Intuitionistic fuzzy sets. *Fuzzy Sets and Systems 20*, 1 (1986), 87-96.

7   Priest, G. Paraconsistent logic. *Handbook of Philosophical Logic*, vol 6, Kluwer, 2002.

8   Bruno, W. Dialetheism, logical consequence and hierarchy. *Analysis 4*, 64 (2004), 318-326.

9   Loeb, P. A. and Wolff, M. P. *Nonstandard Analysis for the Working Mathematician*. Kluwer, 2000.

10   Gonzalez, R.C. and Woods, R.E. *Digital Image Processing*. 3rd ed. Prentice Hall, 2007.

11   Deshmukh, K.S. and Shinde, G.N. An adaptive color image segmentation. *Electronic Letters on Computer Vision and Image Analysis 5*, 4 (2005), 12-23.

12   Shapiro, L.G. and Stockman, G.C. *Computer Vision*. Prentice-Hall, 2001.

13   Bezdek, J.C. *Pattern Recognition with Fuzzy Objective Function Algorithms*. New Plemm, 1981.

14   Haralick, R.M. and Shapiro, L.G. Survey: Image segmentation techniques. *Computer Vision, Graphics and Image Processing 1*, 29 (1985), 100-132.

15   V. I. Borisenko, A. A. Zlatopolskii, and I. B. Muchnik, Image segmentation (state-of-the-art survey). *Automation and Remote Control 7*, 48 (1987), 837-879.

16   Pal, N.R. and Pal, S.K. A review in image segmentation techniques. *Pattern Recognition 9*, 26 (1993), 1277-1294.

17   Y. J. Zhang, A survey on evaluation methods for image segmentation. *Pattern Recognition 8*, 29 (1996), 1335-1346.

18   Zhang, H., Fritts, J.E., and Goldman, S.A. Image segmentation evaluation: A Survey of unsupervised methods. *Computer Vision and Image Understanding 2*, 110 (2008), 260-280.

19   Spirkovska, L. *A Summary of Image Segmentation Techniques*. NASA Technical Memorandum, 104022, 1993.

20   Aghbari, Z.A. and Al-Haj, R. Hill-manipulation, An effective algorithm for color image segmentation. *Image and Vision Computing 24*, 8 (2006), 894-903.

21   Bleau, A. and Leon, L.J. Watershed-based segmentation and region merging. *Computer Vision and Image Understanding 3*, 77 (2000), 317-370.

22   Jiang, Y. and Zhou, Z.-H. SOM ensemble-based image segmentation. *Neural Processing Letters 3*, 20 (2004), 171-178.

23   Yu, Z., Zou, T., and Yu, S. A modified fuzzy C-Means algorithm with adaptive spatial information for color image segmentation. *Computational Intelligence for Image Processing*, 2009, 48-52.

24   Glasbey, C.A. An analysis of histogram-based thresholding algorithms. *Graphical Models and Image Processing 6*, 55 (1993), 532-537.

25   Kapur, J.N., ahoo, P.K., and Wong, A.K.C. A new method for graylevel picture thresholding using the entropy of the histogram. *Computer Vision Graphics, and Image Processing 3*, 29 (1985), 273-285.

26   Alvarez, L., Lions, P.L., and Morel, J.-M. Image selective smoothing and edge detection by nonlinear diffusion, II. *SIAM Journal on Numerical Analysis 29*, 3 (1992), 845-866.

27   Pollak, I., Willsky, A.S., and Krim, H. Image segmentation and edge enhancement with stabilized inverse diffusion equations. *IEEE Trans. on Image Processing 2*, 9 (2000), 256-266.

28 Tabb, M. and Ahuja, N. Multiscale image segmentation by integrated edge and region detection. *IEEE Trans. on Image Processing 5*, 6 (1997), 642-655.

29 Freixenet, J., Muñoz, X., Raba, D., Martí, J., and Cufí, X. Yet another survey on image segmentation: Region and boundary information integration. *Lecture Notes in Computer Science* 2352 (2002), 408 - 422.

30 Campbell, J.G., Fraley, C., Murtagh, F., and Raftery, A.E. Linear flaw detection in woven textiles using model-based clusterin. *Pattern Recognition Letters 14*, 18 (1997), 1539-1548.

31 Murtagha, F., Rafteryb, A.E., Starck, J.-L. Bayesian inference for multiband image segmentation via model-based cluster trees. *Image and Vision Computing 6*, 23 (2005), 587-596.

32 Najman, L. and Schmitt, M. Watershed of a continuous function. *Signal Processing (Special Issue on Mathematical Morphology) 1* 38 (1994), 99-112.

33 Cousty, J., Bertrand, G., Najman, L., and Couprie, M. Watershed cuts: Minimum spanning forests and the drop of water principle. *IEEE Trans. on Pattern Analysis and Machine Intelligence 8*, 31 (2009), 1362–1374.

34 Tann, H., Gelfand, S., and Delpf, E. A comparative cost function approach to Edge Detection. *IEEE Trans. On Systems, Man, And Cybernetics 6*, 19 (1989).

35 Najman, L. and Schmitt, M.Watershed of a continuous function. *Signal Processing (Special Issue on Mathematical Morphology.) 1*, 38 (1994), 99-112.

36 Najman, L. and Schmitt, M. Geodesic saliency of watershed contours and hierarchical segmentation. *IEEE Trans. on Pattern Analysis and Machine Intelligence 12*, 18 (1996), 1163-1173.

37 Najman, L., Couprie, M., and Bertrand, G.Watersheds, mosaics, and the emergence paradigm. *Discrete Applied Mathematics 2-3*, 147 (2005), 301-324.

38 Li, P. and Xiao, X. Multispectral image segmentation by a multichannel watershed-based approach. *International Journal of Remote Sensing 19*, 28 (2007), 4429-4452.

39 Wang, D. A multiscale gradient algorithm for image segmentation using watersheds. *Pattern Recognition 12*, 30 (1997), 2043-2052.

40   Cheng, H.D. and Chen, J.R. Automatically determine the membership function based on the maximum entropy principle. *Information Sciences 3-4*, 96 (1997), 163-182.

41   Cheng, H.D., Wang, J.L., and Shi, X.J. Microcalcification detection using fuzzy logic and scale space approach. *Pattern Recognition 2*, 37 (2004), 363-375.

42   Cheng, H.D. and Li, J.G. Fuzzy homogeneity and scale space approach to color image aegmentation. *Pattern Recognition* 35 (2002), 373-393.

43   Pal, S.K. and Majumder, D.K.D. *Fuzzy Mathematical Approach to Pattern Recognition*. Wiley, 1986.

44   H. D. Cheng, H. Xu, A Novel fuzzy logic approach to contrast enhancement. *Pattern Recognition*, *5*, 33 (2000), 809-919.

45   Ross, T. *Fuzzy Logic with Engineering Applications*, 3rd ed. Wiley, 2010.

46   Vincent, L. and Soille, P. Watersheds in digital spaces: an efficient algorithm based on immersion simulations. *IEEE Trans. on Pattern Analysis and Machine Intelligence 6*, 13 (1991), 583-598.

47   Beucher, S. and Meyer, F. The morphological approach to segmentation: the watershed transformation. *Mathematical Morphology in Image Processing* (1993), 433-481.

48   Meer, P. and Georgescu, B. Edge detection with embedded confidence. *IEEE Trans. on Pattern Analysis and Machine Intellelligence 12*, 23 (2001), 1351-1356.

49   Robust Image Understanding Lab. 2002. http://coewww.rutgers.edu/riul/research/ code/EDISON/doc/overview.html. May 5, 2009.

50   Comaniciu, D. and Meer, P. Mean shift: A robust approach toward feature space analysis. *IEEE Trans. on Pattern Analysis and Machine Intelligence 5*, 24 (2002), 603-619.

51   Lin, Y.C., Tsai, Y.P., Hung, Y.P., and Shih, Z.C. Comparison between immersion-based and toboggan-based watershed image segmentation. *IEEE Trans. on Image Processing 3*, 15 (2006), 632-640.

52   Garcia, M., Jemal, A., Ward, E., Center, M., Hao, Y., Siegel, R., and Thun, M. *Global Cancer Facts & Figures 2007*. American Cancer Society, 2007.

53   American Cancer Society. *Cancer Facts & Figures 2008*. American Cancer Society, 2008.

54   Jemal, A. Murray, T., Ward, E., Samuels, A., Tiwari, R.C., A. Ghafoor, A., Feuer, E.J., and Thun, M.J. Cancer statistics 2008. *CA: Cancer J. for Clinicians 58*, 2 (2008), 71-96.

55   Jemal, A., Siegel, R., Xu, J., and Ward, E. Cancer statistics 2010. *CA: Cancer J. for Clinicians 60*, 5 (2010), 1-24.

56   American Cancer Society. *Cancer Facts & Figures 2009*. American Cancer Society, 2009.

57   Cheng, H.D., Cai, X.P., Chen, J.W., Hu, L.M., and Lou, X.L. Computer-aided detection and classification of microcalcifications in mammograms: A survey. *Pattern Recognition 12*, 36 (2003), 2967-2991.

58   Cheng, H.D., Shi, X.J., Min, R., Hu, L.M., Cai, X.P., Du, H.N. Approaches for automated detection and classification of masses in mammograms. *Pattern Recognition*,*4*, 39 (2006), 646-668.

59   Joseph, Y.L. and Carey, E.F. Application of artificial neural networks for diagnosis of breast cancer. In *Proceedings of the Congress of Evolutionary Computation*, 1999, 1755-1759.

60   Kopans, D.B. The positive predictive value of mammography. *American Journal of Roentgenology 158*, 3 (1992), 521-526.

61   Knutzen, A.M. and Gisvold, J.J. Likelihood of malignant disease for various categories of mammographically detected, nonpalpable breast lesions. *Mayo Clinic Proceedings*, *68*, 5 (1993), 454-460.

62   Breastcancer.org. Ultrasound. 2009. http://www.breastcancer.org/symptoms/ testing/types/ultrasound.jsp. Jan. 2009.

63   Breastcancer.org. Mammography: Benefits, Risks, What You Need to Know. 2008. http://www.breastcancer.org/symptoms/testing/types/mammograms/ benefits_risks.jsp. Jan. 2009.

64   Jackson, V.P., Hendrick, R.E., Feig, S.A., and Kopans, D. Imaging of the radiographically dense breast. *Radiology 188*, 2 (1993), 297-301.

65   Sivaramakrishna, R., Powell, K.A., Lieber, M.L., Chilcote, W. and Shekhar, R.Texture analysis of lesions in breast ultrasound images. *Computerized Medical Imaging and Graphics 26*, 5 (2002), 303-307.

66   Drukker, K., Giger, M.L., Horsch, K., Kupinski, M.A., Vyborny, C.J., and Mendelson, E.B. Computerized lesion detection on breast ultrasound. *Medical Physics 7*, 29 (2002), 1438-1446.

67   Taylor, K., Merritt, C., Piccoli, C., R. Schmidt, R., G. Rouse, G., B. Fornage, B., E. Rubin, E., D. Georgian-Smith, D., Winsberg, F., Goldberg, B., and Mendelson, E. Ultrasound as a complement to mammography and breast examination to characterize breast masses. *Ultrasound in Medicine and Biology 28*, 1 (2002), 19-26.

68   Bassett, L.W., Ysrael, M., Gold, R.H., and Ysrael, C. Usefulness of mammography and sonography in women less than 35 years of age. *Radiology 180*, 3 (1991), 831.

69   John, C., Blohmer, J.U., and Hamper, U.M. Breast Ultrasound: A Systematic Approach to Technique and Image Interpretation. *Thieme*, 1999.

70   Laine, H., Rainio, J., Arko, H., and Tukeva, T. Comparison of breast structure and findings by X-ray mammography, ultrasound, cytology and histology: A retrospective study. *European Journal of Ultrasound 2*, 2 (1995), 107-115.

71   Jackson, V.P. The role of ultrasound in breast imaging. *Radiology 177*, 2 (1990), 305-311.

72   Wikipedia. Medical imaging. http://en.wikipedia.org/wiki/Medical_image_ processing#Ultrasound. Jan. 2009.

73   Hu, L.M., Cheng, H.D., Zhang, M. A high performance edge detector based on fuzzy inference rules. *Information Sciences 21*, 177 (2007), 4768-4784.

74   Guo, Y.H., Cheng, H.D.,Tian, J, and Zhang, Y.T. A novel approach to speckle reduction in ultrasound imaging. *Ultrasound in Medicine and Biology 4*, 35 (2009), 628-640.

75   Chang, R.F., Wu, W.J., Moon, W.K., and Chen, D.R. Improvement in breast tumor discrimination by support vector machines and speckle-emphasis texture analysis. *Ultrasound in Medicine and Biology 5*, 29 (2003), 679-686.

76   Alemán-Flores, M., Álvarez, L., and Caselles, V. Texture-oriented anisotropic filtering and geodesic active contours in breast tumor ultrasound segmentation. *Journal of Mathematical Imaging and Vision 1*, 28 (2007), 81-97.

77   Yeh, C.-K., Chen, Y.-S., Fan, W.-C., and Liao, Y.-Y. A disk expansion segmentation method for ultrasonic breast lesions. *Pattern Recognition 5*, 42 (2009), 596-606.

78   Noble, J.A. and Boukerroui, D. Ultrasound image segmentation: A survey. *IEEE Trans. on Medical Imaging 8*, 25 (2006), 987-1010.

79   Duta, N. and Sonka, M. Segmentation and interpretation of MR brain images: An improved active shape model. *IEEE Trans. Medical Imaging 6*, 17 (1998), 1049-1062.

80   Mignotte, M., Meunier, J., and Tardif, J.C. Endocardial boundary estimation and tracking in echocardiographic images ssing deformable template and Markov random fields. *Pattern Analysis and Applications 4*, 4 (2001), 256-271.

81   Hao, X., Bruce, C.J., Pislaru, C., and Greenleaf, J.F. Segmenting high-frequency intracardiac ultrasound images for myocardium into infarcted, ischemic and normal regions. *IEEE. Trans. on Medical Imaging 122*, 20 (2001), 1373–1383.

82   Madabhushi, A. and Metaxas, D.N. Combining low-, high-level and empirical domain knowledge for automated segmentation of ultrasonic breast lesions. *IEEE Trans. on Medical Imaging 2*, 22 (2003), 155-169.

83   Montagnat, J., Sermesant, M., Delingette, H., Malandain, G., and Ayache, N. Anisotropic filtering for model-based segmentation of 4-D cylindrical echocardiographic images. *Pattern Recognition Letters 4-5*, 24 (2003), 815-828.

84   Ashton, E.A. and Parker, K.J. Multiple resolution Bayesian segmentation of ultrasound images. *Ultrasound Image 17*, 4 (1995), 291-304.

85   Boukerroui, D., Baskurt, A., Noble, J.A., and Basset, O. Segmentation of ultrasound images multiresolution 2D and 3D algorithm based on global and local statistics. *Pattern Recognition Letters 12*, 24 (2003), 1373-1383.

86   Mousa, R., Munib, Q., and Moussa, A. Breast cancer diagnosis system based on wavelet analysis and fuzzy-neural. *Expert Systems With Applications 4*, 28 (2005), 713-723.

87   Kirberger, R.M. BVSc, mmedVet, Imaging artifacts in diagnostic ultrasound-A Review. *Veterinary Radiology & Ultrasound 4*, 36 (2005), 297 - 306.

88   Paragios, N. and Deriche, R. Geodesic active contours and level sets for the detection and tracking of moving objects. *IEEE Trans. on Pattern Analysis Machine Intelligence 3*, 22 (2000), 266-280.

89   Chalana, V. and Kim, Y. A methodology for evaluation of boundary detection algorithms on medical images. *IEEE Trans. on Medical Imaging 5*, 16 (1997), 642-652.

90   Kim, U.H., Seo, B.K., Lee, J., Kim, S.J., Cho, K.R., and Lee, K.Y. Correlation of ultrasound findings with histology, tumor grade, and biological markers in breast cancer. *Acta Oncologica 8*, 47 (2008), 1531-1538.

91   Chan, T.F. and Vese, L.A. Active contours without edges. *IEEE Trans. on Image Processing 2*, 10 (2001), 266-277.

92   Chan, T.F. and Vese, L.A. A multiphase level set framework for image segmentation using the Mumford and Shah model. *International J. of Computer Vision 50*, 3 (2002), 271-293.

93   Chen, D.R., Chang, R.F., Wu, W.J., Moon, W.K., and Wu, W.L. 3-D Breast ultrasound segmentation using active contour model. *Ultrasound Medicine and Biology 7*, 29 (2003), 1017-1026.

94   Liu, B., Cheng, H.D., Huang, J.H., Tian, J.W., Tang, X.L., and Liu, J.F. Fully automatic and segmentation-robust classification of breast tumors based on local texture analysis of ultrasound images. *Pattern Recognition 1*, 43 (2010), 280-298.

95   Cheng, H.D., Shan, J., Ju, W., Guo, Y.H., and Zhang, L. Automated breast cancer detection and classification using ultrasound images: A survey. *Pattern Recognition 1*, 43 (2010), 299-317.

96   Warfield, S.K., Zou, K.H., Kaus, M.R., and Wells, W.M. Simultaneous validation of image segmentation and assessment of expert quality. In *Proceedings IEEE International Symposium on Biomedical Imaging*, 2002, 94–97.

97   Cheng, H.D., Jiang, X.H., Sun, Y., and Wang, J.L. Color image segmentation: Advances and prospects. *Pattern Recognition 12*, 34 (2001), 2259-2281.

98   Mao, X., Zhang, Y., Hu, Y., and Sun, B. Color image segmentation method based on region growing and ant colony clustering. *IEEE Computer Society 1* (2009), 173-177.

99   Special issue on digital libraries: representation and retrieval. *IEEE Trans. on Pattern Analysis and Machine Intelligence*, *8*, PAMI-18 (1996).

100   Special issue on segmentation, description, and retrieval of video content. *IEEE Trans. on Circuits and Systems for Video Technology*, *5*, CASVT-8 (1998).

101   Pietikainen, M. Accurate color discrimination with classification based on feature distributions. In *International Conference on Pattern Recognition*, 1996, 833-838.

102   Littmann, E. and Ritter, H. Adaptive color segmentation --a comparison of neural and statistical methods. *IEEE Trans. on Neural Networks 8*, 1 (1997), 175-185.

103   Huntsberger, T.L., Jacobs, C.L., and Cannon, R.L. Iterative fuzzy image segmentation. *Pattern Recognition 18*, 2 (1985), 131-138.

104   Kim, W.S. and Park, R.H. Color image palette construction based on the HSI color system for minimizing the reconstruction error. In *IEEE International Conference on Image Processing*, 1996, 1041-1044.

105   Hoy, D.E.P. On the use of color imaging in experimental applications. *Experimental Techniques 21*, 4 (1997), 17-19.

106   Robinson, G.S. Color edge detection. *Optical Engeering 16*, 5 (1997), 479-484.

107   Tseng, D.C. and Chang, C.H. Color segmentation using perceptual attributes. In *IEEE International Conference on Pattern Recognition*, 1992, 228-231.

108   Pal, S.K. A review on image segmentation techniques. *Pattern Recognition 29*, (1993), 1277-1294.

109   Yang, C.K. and Tsai, W.H. Reduction of color space dimensionality by moment-preserving thresholding and its application for edge detection in color images,. *Pattern Recognition Letters 5*, 17 (1996), 481-490.

110   Tremeau, A. and Borel, N. A region growing and merging algorithm to color segmentation. *Pattern Recognition 7*, 30 (1997), 1191-1203.

111   Kato, Z. and Pong, T. A Markov random field image segmentation model for color textured images. *Image and Vision Computing 10*, 24 (2006), 1103-1114.

112   Littmann, E. and Ritter, H. Adaptive color segmentation - a comparison of neural and statistical methods,. *IEEE Trans. on Neural Networks 8*, 1 (1997), 175-185.

113   Fu, K.S. and Mui, J.K. A survey on image segmentation. *Pattern Recognition 13*, 1 (1981), 3-16.

114   Macaire, L., Ultre, V., and Postaire, J.-G. Determination of compatibility coe$cients for color edge detection by relaxation. In *International Conference on Image Processing*, (1996), 1045-1048.

115   Nevatia, K. A color edge detector and its use in scene segmentation. *IEEE Trans. on Systems, Man Cybernetics 11*, 7 (1977), 820-826.

116   Trahanias, P.E. and Venetsanopoulos, A.N. Color edge detection using vector order statistics. *IEEE Trans. Image Processing 2*, 2 (1993), 259-265.

117   Trahanias, P.E. and Venetsanopoulos, A.N. Vector order statistics operators as color edge detectors. *IEEE Trans. Systems Man Cybernet.-Part B: Cybernetics 26*, 1 (1996), 135-143.

118   Ohta, Y., Kanade, T., and Sakai, T. Color information for region segmentation. *Computer Graphics Image Processing 3*, 13 (1980), 222-241.

119   Ohlander, R., Price, K., and Reddy, D.R. Picture segmentation using a recursive region splitting method. *Computer Graphics Image Processing 3*, 8 (1978), 313-333.

120   Tominaga, S. Color image segmentation using three perceptual attributes. In *Proceedings of the IEEEConference on Computer Vision and Pattern Recognition*, 1986, 628-630.

121   Lescure, P., Meas-Yedid, V., Dupoisot, H., and Stamon, G. Color segmentation on biological microscope images. In *Proceeding of SPIE, Application of Artificial Neural Networks in Image Processing IV*, (1999), 182-193.

122   Rae, R. and Ritter, H.J. Recognition of human head orientation based on artificial neural networks. *IEEE Trans. on Neural Network*, *9*, 2 (1998), 257-265.

123   C.-L. Huang, Pattern image segmentation using modified Hopfield model. *Pattern Recognition Letters*, *3*, 15 (1999), 345-353.

124   Campadelli, P., Medici, D., and Schettini, R. Color image segmentation using Hopfield networks. *Image Vision Computing 3*, 15 (1997), 161-166.

125   Vesanto, J. and Alhoniemi, E. Clustering of the self-organizing map. *IEEE Trans. on Neural Networks 11*, 3 (2000), 586-600.

126   Ji, S. and Park, H.W. Image segmentation of color image based on region coherency. In *International Conference on Image Processing*, 1998, 80-83.

127   Lo, Y.S. and Pei, S.C. Color image segmentation using local histogram and self-organization of Kohonen feature map. In *International Conference on Image Processing*, 1999, 232-239.

128   Keller, J.M.,Gray, M.R., and Givens, J.A. A fuzzy K-nearest neighbor algorithm. *IEEE Trans. on Systems, Man Cybernetics 4*, SMC-15 (1985), 580-585.

129   Keller, J.M. and Carpenter, C.L. Image segmentation in the presence of uncertainty. *International Journal of Intelligent Systems 2*, 5 (1990), 193-208.

130   Bezdek, J.C. and Castelaz, P.F. Prototype classification and feature selection with fuzzy sets. *Pattern Recognition Letters 14*, (1993), 483-488.

131   Nock, R. and Nielsen, F. Semi-supervised statistical region refinement for color image segmentation. *Pattern Recognition 6*, 38 (2005), 835-846.

132   Robinson, G. Color edge detection. *Optical Engineering 16*, 5 (1977), 479-484.

133   Fairchild, M.D. *Color Appearance Models*. Addison-Wesley, 1998.

134   Ruspini, E. Numerical methods for fuzzy clustering. *Information Sciences 3*, 2 (1970), 319-350.

135   Dunn, J.C. A fuzzy relative of the ISODATA process and its use in detecting compact, well separated clusters. *Cybernetics 3*, 3 (1974), 95-104.

136   Cheng, H.D. and Li, J. Fuzzy homogeneity and scale-space approach to color image segmentation. *Pattern Recognition 7*, 36 (2003), 1545-1562.

CURRICULUM VITAE

Ming Zhang
(November, 2010)

EDUCATION

Ph.D., Computer Science   12/ 2010

Utah State University, Logan, UT   GPA 3.9

Advisor: Prof. Heng-Da Cheng

B.Eng., Computer Science   07/2001

Shandong University, Jinan, Shandong, China   GPA 3.8

RESEARCH INTERESTS

Computer Vision   Pattern Recognition

Image Processing   Medical Image Processing

Fuzzy Logic   Neutrosophy

RESEARCH AND WORK EXPERIENCE

Teaching Assistant   08/2004 – present

School of Computer Science, Utah State University   Logan, UT

- Graded computer algorithms, parallel computing, digital image processing,

  software engineering, and pattern recognition.

- Tutored all levels of computer science undergraduate students.

System Administrator 06/2006 – 12/2008

Department of Economics, Utah State University Logan, UT

- Managed department servers (DNS, email, ftp, backup) and department computers.

- Protected computers from being attacked.

Group member of CVPRIP lab 04/2005 – present

School of Computer Science, Utah State University Logan, UT

- Research on breast cancer segmentation and classification in CVPRIP (Computer Vision, Pattern Recognition, Image Processing) Lab. The research is for breast cancer mass detection based on ultrasound images.

- Introduced neutrosophy to ultrasound image processing.

- Designed and implemented pavement crack detection system, a real-time system created to detect cracks in asphalt and concrete roads.

- Designed and implemented vehicle detection and classification system. It uses a model-based method to develop an automatic video-based intelligent feature extraction system. The images were captured by the highway traffic control office of Utah Department of Transportation (UDOT).

Software Programmer 07/2001 – 09/2003

Xu Ji Company Jinan, China

- Created power plant information collecting system. The system uses palm to collect the diagonal information within the power plant per hour and transfer them to the corresponding departments.

- Pre-designed a call center system which serves as customer service for the Power Bureau.

Internship   02/2001 – 07/2001

Xian Dai Company   Jinan, China

- Implemented work sheet system for power plants

Research Assistant   09/1998 – 07/2000

Shandong University   Jinan, China

- Served as research assistant in EBM (Electron Beam) Lab

- Participated in developing diagnostic system for diesel engine status

- Participated in developing the Automatic Check system for vehicle headlight

- Provided computer maintenance

Conference Reviewer

- Reviewed papers of 8th Joint Conference on Information Science   03/2005

- Reviewed papers of 11th Joint Conference on Information Science   03/2008

AWARDS AND HONORS

- Teaching Assistant, *Computer Science,* 2004 – present

- Dissertation Fellowship, 2008 – 2009

- Graduate Studies Honor Roll, 2003 – 2004

- Vice Presidential Fellowship, 2003 – 2004

- Scholarship Recipient, 1997 – 1998, 1998 – 1999, 1999 – 2000, 2000 – 2001

- Ping Pong Champion, *Utah State University*, 2003 – 2007

SELECTED PUBLICATIONS

<u>Journals</u>

- **Zhang, M.**, Cheng, H. D., Color Segmentation Based on Neutrosophic Method, Pattern Recognition, (under review).

- **Zhang, M.**, Zhang, L., Cheng, H. D., Segmentation of Breast Ultrasound Images Based on Neutrosophic Method, Optical Engineering, (in press).

- **Zhang, M.**, Zhang, L., Cheng, H. D., A Neutrosophic Approach to Image Segmentation Based on Watershed Approach, Signal Processing, 90(5), 1510-1517, 2010

- Cheng, H. D., Min, R., **Zhang, M.**, Automatic Wavelet base selection and its application to contrast enhancement, Signal Processing, 90(4), 1279-1289, 2010

- Hu, L.M., Cheng, H. D., **Zhang, M.**, A High Performance Edge Detector Based on Fuzzy Inference Rules, Information Science, 177(21): 4768-4784, 2007

- Cheng, H. D., Xue, M., Shi, X. J., **Zhang, M.**, Novel Contrast Enhancement Approach Based on Fuzzy Homogeneity, Optical Engineering, 46(4), 047002, 2006.

- **Zhang, M.**, Study on Conductivity Measurement of Metal with High Temperature, Measurement Technique, No. 6, 6-8, June 2002 (in Chinese).

<u>Conferences</u>

- Zhang, L., **Zhang, M.**, An Extended Fuzzy Logic Method for Watershed, Proc. 11th Join Conference of Information Science, 2008.

- **Zhang, M.**, Zhang, L., Fuzzy Watershed Method for Image Segmentation, Proc. 10th

Join Conference of Information Science, 2007.

- Zhang, L., Sun, Y., **Zhang, M.,** Lightweight RTPS Middleware for Distributed SCADA System, Proc. 10th Join Conference of Information Science, 2007.